

RESEARCH ARTICLE

10.1002/2013JC009648

Key Points:

- Merging scatterometers with radiometers to create a long time series is presented
- Low-moderate winds constitute 98% of daily mean winds and are best to retrieve
- Wind retrieval differences under high winds and rain challenge the synthesis

Correspondence to:

L. Yu,
lyu@whoi.edu

Citation:

Yu, L., and X. Jin (2014), Insights on the OAF flux ocean surface vector wind analysis merged from scatterometers and passive microwave radiometers (1987 onward), *J. Geophys. Res. Oceans*, 119, 5244–5269, doi:10.1002/2013JC009648.

Received 30 NOV 2013

Accepted 18 JUL 2014

Accepted article online 25 JUL 2014

Published online 19 AUG 2014

Insights on the OAF flux ocean surface vector wind analysis merged from scatterometers and passive microwave radiometers (1987 onward)

Lisan Yu¹ and Xiangze Jin¹¹Department of Physical Oceanography, Woods Hole Oceanographic Institution, Woods Hole, Massachusetts, USA

Abstract A high-resolution global daily analysis of ocean surface vector winds (1987 onward) was developed by the Objectively Analyzed air-sea Fluxes (OAF flux) project. This study addressed the issues related to the development of the time series through objective synthesis of 12 satellite sensors (two scatterometers and 10 passive microwave radiometers) using a least-variance linear statistical estimation. The issues include the rationale that supports the multisensor synthesis, the methodology and strategy that were developed, the challenges that were encountered, and the comparison of the synthesized daily mean fields with reference to scatterometers and atmospheric reanalyses. The synthesis was established on the bases that the low and moderate winds ($<15 \text{ m s}^{-1}$) constitute 98% of global daily wind fields, and they are the range of winds that are retrieved with best quality and consistency by both scatterometers and radiometers. Yet, challenges are presented in situations of synoptic weather systems due mainly to three factors: (i) the lack of radiometer retrievals in rain conditions, (ii) the inability to fill in the data voids caused by eliminating rain-flagged QuikSCAT wind vector cells, and (iii) the persistent differences between QuikSCAT and ASCAT high winds. The study showed that the daily mean surface winds can be confidently constructed from merging scatterometers with radiometers over the global oceans, except for the regions influenced by synoptic weather storms. The uncertainties in present scatterometer and radiometer observations under high winds and rain conditions lead to uncertainties in the synthesized synoptic structures.

1. Introduction

The NASA Seasat-A Satellite scatterometer (SASS) launched in June 1978 was a proof-of-concept mission to demonstrate that ocean surface vector wind could be retrieved from a spaceborne scatterometer [Jones *et al.*, 1982]. The success of the SASS has inspired the development of a series of satellite scatterometer missions in the decades that followed. To date, nine scatterometers have been launched, including the European Remote sensing Satellite (ERS)–1 (1992–1996) and ERS-2 (1995–2000) operated by the European Space Agency [Attema, 1991], the NASA Scatterometer (NSCAT) aboard the Japanese National Space Development Agency (NASDA) Advanced Earth Observing Satellite I (ADEOS-I; 9 months, 1996–1997) [Naderi *et al.*, 1991], the NASA SeaWinds-1 scatterometer on the QuikSCAT satellite (1999–2009) and the SeaWinds-2 on NASDA ADEOS-II (10 months, 2002–2003) [Spencer *et al.*, 2000], the Advanced Scatterometer (ASCAT)-A on MetOp-A (2006 onward) and ASCAT-B on MetOp-B (2012 onward) operated by the European Organization for the Exploitation of Meteorological Satellites (EUMETSAT) [Figa-Saldaña *et al.*, 2002], OceanSat-2 Scatterometer (OSCAT; 2009–2014) launched by the Indian Space Research Organization (ISRO) [Padia, 2010; Verhoef and Stoffelen, 2012], and the scatterometer onboard the NASA Aquarius/SAC-D satellite (2009 onward) [Yueh and Chubb, 2012]. As to this writing, only three scatterometers, namely, ASCAT-A, ASCAT-B, and Aquarius, are operating.

Ocean surface winds are an Essential Climate Variable (ECV) identified by the Global Climate Observing System (GCOS) [GCOS, 2010]. Climate studies need more than ever a consistent long-term record of ocean surface vector winds to characterize and understand the change in ocean surface winds, as winds are involved in virtually every aspect of air-sea feedback and interaction. The scientific requirements for satellite-based long-term ocean vector wind records have been articulated in the GCOS Climate Monitoring Principles for satellite measurements. However, a single scatterometer is not sufficient to address the requirements. The data record provided by the nine scatterometers that have been launched ranges from 9 months to 10

years, which renders the need to integrate the discrete data records and create a unified long time series over the lifespans of all missions. Merging the scatterometers from different missions is technically challenging, because the differences in the operating frequency used by different scatterometers give rise to different characteristics in retrievals. The European scatterometers, such as ERS-1/2 and the ASCAT series, operate at the C-band (5.3 GHz) and have a relatively narrow swath and are less sensitive to rain [Portabella and Stoffelen, 2009]. The NASA scatterometers, such as NSCAT, SeaWinds, and QuikSCAT, as well as the Indian OSCAT, use the Ku-band (13.4 GHz) that allows a larger swath but is more subjective to rain contamination. The recent Aquarius scatterometer that operates at the L-band (1.4 GHz) further adds up to the range of scatterometer retrievals. The operating frequency affects directly the sensor's swath size and sensitivity to rain, which are two key parameters in determining the spatial and temporal resolutions at which the scatterometer records can be unified.

The temporal resolution is the first major issue when considering the coverage provided by each scatterometer. The Ku-band QuikSCAT (1999–2009) has so far provided the longest record of global scatterometer data yet obtained, with a 93% global coverage every 24 h. The C-band ASCAT-A/B together with the Ku-band OSCAT scatterometers have demonstrated significant capability of filling the void left by the loss of QuikSCAT. However, for the pre-QuikSCAT period, the C-band ERS-1/2 are the only scatterometers that have sufficiently long records. These two sensors have a narrow swath of 500 km, which limits the daily coverage to 40% of the global ocean and requires 3 days to provide almost full coverage. It appears that there is no straightforward approach to reconcile the coverage differences between the C-band and Ku-band retrievals, if no additional satellites are introduced.

Efforts have been made in the past 5 years by the Objectively Analyzed air-sea Fluxes (OAFlux) project at the Woods Hole Oceanographic Institution (WHOI) to develop a satellite-based ocean vector wind time series by utilizing the rich surface wind speed database established by passive microwave radiometers as a means to improve the data coverage of scatterometers and improve the quality of the time series. Albeit a wind speed only sensor, the six-sensor series of the Special Sensor Microwave/Imager (SSM/I) on the Defense Meteorological Satellite Program (DMSP) that were launched subsequently on different platforms starting from July 1987 [Hollinger et al., 1990; Wentz, 1997], together with the follow-on Special Sensor Microwave Imager/Sounder (SSMIS) sensors [Kunkee et al., 2008] that have been in operation since 2005, constitute a continuous and reliable data record of global wind speed for 26 years and continuing. In addition to the SSM/I and SSMIS series, the database of satellite wind speed data records is further augmented by the launch of the Tropical Rainfall Measuring Mission (TRMM) Microwave Imager (TMI) [Wentz et al., 2001] in November 1997, the Advanced Microwave Scanning Radiometer-Earth Observing System (AMSRE) in May 2002 [Meissner and Wentz, 2002], and the WindSat Polarimetric Radiometer in January 2003. WindSat is a new type of passive microwave sensor that is equipped with an ability of retrieving both ocean wind speed and vector (above 8 m s^{-1}) through measuring the complex correlation between vertically and horizontally polarized microwave radiation [Gaiser et al., 2004].

In this study, the OAFlux high-resolution daily analysis of global ocean surface vector developed from merging scatterometers with radiometers for the period from July 1987 to December 2012 is presented. A total of 12 sensors were used by OAFlux, including two scatterometers (QuikSCAT and ASCAT) and 10 radiometers (six SSM/I sensors, two SSMIS sensors, AMSRE, and WindSat) using a least-variance linear statistical estimation. This new unified record of ocean surface vector wind extends the OAFlux existing surface flux database (<http://oafux.whoi.edu>), making it a site of choice for consistent, good quality, multidecadal time series of air-sea heat, moisture, and momentum fluxes [Yu and Weller, 2007; Yu, 2007; Yu, et al., 2008; Yu and Jin, 2012]. We note, however, that the 0.25° gridded OAFlux vector wind product was constructed on a daily basis, based primarily on the consideration of the maximum data coverage throughout the analysis period. The caveat of such a product is its inability to resolve surface wind variability on diurnal timescales and on spatial scales associated with subdaily atmospheric dynamics on the mesoscales. Although scatterometers do resolve the latter spatial variability, no single scatterometer or radiometer can fully resolve the diurnal variability. Creating a synthesized product that has a temporal resolution better than the capability of the individual sensor without sacrificing the accuracy is a research challenge yet to be overcome. In addition, no single data product can cater to the demand of all the research needs. The OAFlux daily vector wind product aims at providing a long-term daily mean representation for the period that the combined use of scatterometers and radiometers can provide near-global coverage for the majority of the days. The OAFlux

surface vector wind, heat flux, and evaporation products on daily resolution have been used in a broad range of research applications [Syed *et al.*, 2010; Hansen *et al.*, 2012; Peterson *et al.*, 2012; Trenberth and Fasullo, 2012; Romanou *et al.*, 2013; Kelly and Dong, 2013] on timescales including synoptic (several days) [e.g., Joyce *et al.*, 2009], seasonal [e.g., Yu, 2011], intraseasonal [e.g., Johnson and Ciesielski, 2013], interannual [e.g., Katsura *et al.*, 2013], and decadal and multidecadal [e.g., Skliris *et al.*, 2014]. As the global climate has been and continues to be changing, the scientific values of a continuous and consistent daily surface vector wind time series from 1987 onward are yet to be discovered.

High-quality satellite wind time series are highly desired by the community to characterize and gain improved understanding of climate trends and variability particularly in sea surface height (SSH), sea surface temperature (SST), and sea surface salinity (SSS) that are observed by satellites and in situ platforms and to provide a reference for assessing climate model simulations [e.g., Freilich and Dunbar, 1999; Mears *et al.*, 2001; Kelly *et al.*, 2001; Portabella and Stoffelen, 2001; Stiles and Yueh, 2002; Ebuchi *et al.*, 2002; Bourassa *et al.*, 2003; Milliff *et al.*, 2004; Chelton and Freilich, 2005]. In particular, QuikSCAT established not only an optimum benchmark with respect to the Ku-band scatterometry [Brown, 1979; Plant, 1986] but also an important 10 year climatology of high-quality ocean wind observations [Vogelzang *et al.*, 2011; Karagali *et al.*, 2013, 2014] that have benefited meteorologists and oceanographers tremendously for weather and climate research and applications on a broad range of timescales. Parallel efforts on utilizing satellite observations from multiple sensors from multiple satellite platforms have been made by several groups [e.g., Atlas *et al.*, 1996, 2011; Chin *et al.*, 1998; Bentamy *et al.*, 2002]. Together with the latest atmospheric reanalysis efforts, there is a rich list of satellite-derived and atmospheric reanalyzed surface wind products for use. Different methodologies used by different groups would lead to differences in the resulting wind time series and define the spatial and temporal ranges of the applicability of the data products. Thus, it is important that the methodology and strategy used in developing each surface wind product are justifiable from both theoretical and technical considerations.

This study addresses the methodology and approaches that we have employed and the challenging technical issues that we have tackled during developing the OAFflux multisensor synthesis. Given that scatterometers and microwave radiometers (section 2) measure different electromagnetic properties at the ocean surface, one fundamental issue is to what degree wind retrievals from the two different instruments can be synergized. This report will begin with the rationale that supports the synergy of scatterometers and radiometers (section 3), and then proceed to discuss the methodology and strategy that was developed for the OAFflux objective synthesis (section 4), the challenging issues that were encountered during the synthesis (section 5), and validity of the OAFflux synthesized daily mean fields with reference to scatterometers and atmospheric reanalyses (section 6). A summary and conclusion is given in section 7.

2. Data Description

2.1. Satellite Wind Sensors

There are wind speed and direction data records from nine scatterometers and wind speed data records from 11 passive microwave radiometers (MWRs). Not all were selected by the OAFflux synthesis. The 12 sensors in the OAFflux synthesis include six SSM/I sensors (F08, F10, F11, F13, F14, and F15), two SSMIS sensors (F16 and F17), AMSRE, WindSat, QuikSCAT, and ASCAT-A. As to this writing, ASCAT-B and OSCAT wind retrievals have been validated and tested, and work is underway to include the two scatterometers to strengthen and continue the OAFflux time series. The sensors that were left out of the OAFflux analysis are due either to short data record (e.g., NSCAT and SeaWinds), or to unknown uncertainties in TRMM [DeMoss and Bowman, 2007] and ERS-1/2 [Quilfen *et al.*, 2001], or to limited daily global coverage (e.g., Aquarius and ERS-1/2).

The time line for each of the 12 sensors is shown in Figure 1a and the period of each data set used in the OAFflux synthesis is shown in Figure 1b. A summary of the sensor characteristics and accuracy is given below.

2.1.1. SSM/I

The SSM/I sensor is a seven-channel passive microwave radiometer operating at four frequencies (19.35, 22.235, 37.0, and 85.5 GHz) and dual-polarization (except at 22.235 GHz which is V-polarization only) [Hollinger *et al.*, 1990; Wentz, 1997]. SSM/I covers 75% of the global oceans in 24 h with a swath width of 1394 km.

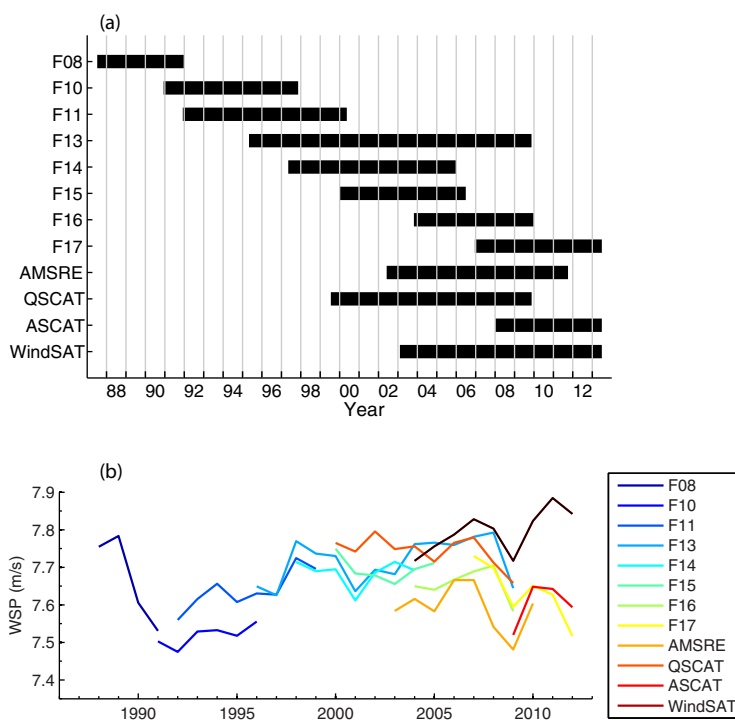


Figure 1. (a) Timeline of the 12 sensors included in the OAFflux synthesis after truncating the periods of abnormality. (b) Annual mean time series of input data sets.

The footprint resolution (along \times cross-track) is $69 \text{ km} \times 43 \text{ km}$ at 19 GHz, $50 \text{ km} \times 40 \text{ km}$ at 22 GHz, $37 \text{ km} \times 28 \text{ km}$ at 37 GHz, and $15 \text{ km} \times 13 \text{ km}$ at 85 GHz. SSM/I was first launched onboard the DMSP F8 satellite on 19 June 1987, and subsequent SSM/I's have been launched on later DMSP satellites (F10, F11, F13, F14, and F15). Wind speed retrievals are available under both clear and cloud conditions but can be contaminated when cloud/rain liquid water values exceeded 18 mg cm^{-2} . Mears *et al.* [2001] showed that mean difference between SSM/I winds and buoy winds is less than 0.5 m s^{-1} and the standard deviation of the difference is around 1.3 m s^{-1} .

2.1.2. SSMIS

The SSMIS sensor is the next-generation SSM/I [Kunkee *et al.*, 2008; Sun and Weng, 2008]. The instrument has 24 channels with discrete frequencies from 19 to 183 GHz and represents the most complex operational satellite passive microwave imager/sounding sensor ever flown. Seven SSMIS channels are designed for imaging that have frequencies similar to SSM/I, except for shifting the SSM/I 85.5 GHz frequency to the 91.655 GHz frequency. The remaining 17 channels are for the temperature/water vapor sounding. The SSMIS sensor has a larger scan angle of 144° compared to 102° for SSM/I and a larger swath with of 1700 km, compared to 1400 km for SSM/I. The conically scanning SSMIS offers 80% of global coverage on daily basis with the footprint resolution varying from $14 \text{ km} \times 13 \text{ km}$ at 183 GHz to $70 \text{ km} \times 42 \text{ km}$ at 19 GHz. The instrument became operational in November 2005 onboard the DMSP F16, with one additional onboard F17 in March 2008. Buoy comparisons based on the observations between November 2003 and July 2005 [Kunkee *et al.*, 2008] showed that the performance of SSMIS F16 was very similar to SSM/I F13, F14, and F15, with the mean difference less than 0.2 m s^{-1} for all sensors and a standard deviation between 1.7 and 1.9 m s^{-1} .

2.1.3. AMSR-E

The AMSR-E sensor was launched on 4 May 2002 onboard the NASA's Aqua spacecraft. It is a 12-channel passive microwave radiometer system with six-frequency channels at 6.9, 10.6, 18.7, 23.8, 36.5, and 89 GHz. The footprint resolution varies from $75 \text{ km} \times 43 \text{ km}$ at 6.9 GHz to $6 \text{ km} \times 4 \text{ km}$ at 89 GHz. The low-frequency channels (6.9 and 10.6 GHz) penetrate deeper and are more sensitive to sea surface temperature and wind but less sensitive to the atmosphere [Meissner and Wentz, 2002]. The SST and wind speed algorithms are essentially the same, except that the SST algorithm uses all five AMSR-E lower-frequency

channels, while the wind algorithm does not use the 6.9 GHz channels. The improved sensitivity of AMSRE to surface wind and temperature improves the accuracy of wind speed retrievals when compared to SSM/I [Meissner and Wentz, 2012]. Additionally, AMSR-E scans conically across a 1445 km swath, providing nearly 100% daily coverage for the ocean areas poleward of 45° north and south latitudes and more than 80% daily coverage for the midlatitudes. Comparison of the collocated AMSR-E and TAO buoy winds yielded a mean difference of 0.3 m s⁻¹ and the standard deviation of the difference of 1.1 m s⁻¹ [Konda et al., 2009].

2.1.4. WindSat

The WindSat onboard the Air Force Coriolis mission, which was launched on 6 January 2003, is the first space-based polarimetric microwave radiometer designed to measure the ocean surface wind vector [Gaiser et al., 2004]. The five channels at 6.8, 10.7, 18.7, 23.8, and 37.0 GHz are similar to those of the AMSR-E sensor except that WindSat does not have an 89 GHz channel. The frequencies at 10.7, 18.7, and 23.8 GHz are fully polarized, and these polarization signals contain a small dependence on wind direction that can be used for wind vector retrievals [Yueh et al., 1995; Laursen and Skou, 2001]. WindSat covers a 1025 km active swath and provide both fore and aft views of the swath. The footprint resolution is 40 km × 60 km at 6.8 GHz, 25 km × 38 km at 10.7 GHz, 15 km × 13 km at 18.7 GHz, 12 km × 20 km at 23.8 GHz, and 8 km × 13 km at 37 GHz. WindSat provides 72% of global coverage on a daily basis, slightly less than SSM/I, SSMIS, AMSRE due to the differences in viewing geometries. One weakness of WindSat is that the wind direction retrievals have large uncertainty and can be substantial when wind speeds are less than 5 m s⁻¹ [Wentz et al., 2005; Quilfen et al., 2007]. Yu and Jin [2012] evaluated WindSat and six other sensors by using 106 buoys, where the daily mean wind speeds are generally between 3 and 12 m s⁻¹. The study found that the RMS differences between WindSat and buoy are less than 1 m s⁻¹ in wind speed but more than 50° in wind direction. The study further showed that WindSat wind direction retrievals differ not only from in situ buoy measurements but also from collocated scatterometer direction retrievals. Thus, OAFlex included only WindSat wind speed retrievals but no direction retrievals.

2.1.5. QuikSCAT

The SeaWinds scatterometer on the NASA's QuikSCAT mission uses a dual-beam, conically scanning antenna operating at a frequency of 13.4 GHz (Ku-band) [Spencer et al., 2000; Hoffman and Leidner, 2005]. Backscatter measurements were collected simultaneously at constant incidence angles of 46° for the inner beam, and 54° for the outer beam, with horizontal and vertical polarizations, respectively. The antenna has an elliptical footprint size of roughly 24 km × 31 km at inner beam. The instrument has an unprecedented large swath width of 1800 km, covering 92% of the global oceans in 24 h, and providing a continuous, high-quality ocean vector wind data record for more than 10 years from 19 June 1999 to 23 November 2009. Wind speed and direction at 10 m above the surface of the water are derived from the backscatter energy. Evaluation of collocated QuikSCAT wind retrievals with collocated buoy/ship measurements showed an RMS difference of roughly 1 m s⁻¹ for wind speed and 20° for wind direction [Ebuchi et al., 2002; Bourassa et al., 2003; Vogelzang et al., 2011; Karagali et al., 2014]. It is worth noting that the error statistics quoted here cannot be met in the nadir part of the swath, where the QuikSCAT geometry is less favorable for both speed and direction measurement and for rain screening [e.g., Portabella and Stoffelen, 2001].

2.1.6. ASCAT

ASCAT is a real-aperture C-band (5.255 GHz) vertically polarized radar with three fan-beam antennas pointing to the left-hand side of the subsatellite track and three fan-beam antennas pointing to the right-hand side [Figa-Saldaña et al., 2002]. It is designed as part of the payloads of the EUMETSAT MetOp series of satellites. MetOp-A is the first in the series and was launched on 19 October 2006, followed by MetOp-B that was launched in November 2012, and MetOp-C that is planned in 2017. This series altogether will provide for at least 15 years of operational scatterometer data sets. The ASCAT fan-beam antennae cover two 550 km wide swaths separated by a 720 km wide gap, providing about 71% of global coverage on a daily basis. Swath is gridded into nodes, with one triplet of averaged backscatter measurements per node. These triplets are localized on the surface of the Earth to a set of nodes on a grid along and across swath. An operational product at spatial resolutions of about 50 or 25–34 km can be generated on a nodal grid of 25 or 12.5 km. The C-band ASCAT has a major advantage over the Ku-band QuikSCAT in that it is much less affected by direct rain effects and can operate in all-weather conditions. Hence, ASCAT has a unique position of providing reliable observations for the most intense and often cloud-covered wind phenomena. ASCAT and QuikSCAT retrievals agree well for wind speeds in low to moderate range, with the accuracy

estimated at 1 m s^{-1} or better for wind speed and 20° for wind direction [Bentamy *et al.*, 2012; Vogelzang *et al.*, 2011]. For higher wind conditions ($>15 \text{ m s}^{-1}$), QuikSCAT wind speeds appear to be higher than ASCAT [e.g., Portabella and Stoffelen, 2009; Bentamy *et al.*, 2012]. This study included ASCAT-A, with efforts of adding ASCAT-B being currently underway.

2.2. Processing and Quality-Checking Satellite Retrievals

The OAF flux synthesis obtained the 25 km Level 2 ASCAT wind vectors from the Physical Oceanography Distributed Active Archive center at the Jet Propulsion Laboratory (<http://podaac.jpl.nasa.gov/>), with the source data [Verspeek *et al.*, 2010] located at the Ocean and Sea Ice Satellite Application Facility web pages (OSI SAF) at the Royal Netherlands Meteorological Institute (KNMI) (www.knmi.nl/scatterometer) [ASCAT Wind Product User Manual, 2012]. The data sets of other sensors on a 25 km swath grid were downloaded from the Remote Sensing Systems (RSS) company (<http://www.remss.com/>). In particular, the SSM/I products were from version 6, SSMIS from version 7, AMSRE from version 7, WindSat from version 7, and QuikSCAT from version 4 [Ricciardulli and Wentz, 2011]. These input wind products have the same the same swath wind vector cell (WVC) spacing of 25 km and were all calibrated as equivalent neutral stability winds at a height of 10 m by each producer separately; that is, they are winds that would be observed at 10 m height were the atmosphere neutrally stratified.

Rain affects all wind retrievals from all microwave sensors but with varying degrees [Tournadre and Quilfen, 2005; Portabella *et al.*, 2012; Weissman *et al.*, 2012]. Rain-contaminated retrievals were discarded by using rain flags embedded in the products. Radiometers provide no wind retrievals whenever rain presents. The land-sea mask in the OAF flux wind analysis was originally taken from the 0.25° daily Optimum Interpolation (OI) SST analysis by Reynolds *et al.* [2007]. The mask was further adjusted by expanding the coastlines 50 km into the sea for pre-QuikSCAT years and 25 km into the sea for the QuikSCAT period. Daily sea-ice mask derived from SSM/I sea-ice concentration [Cavalieri *et al.*, 1999] was downloaded from the National Snow and Ice Data Center. Any grid point that has sea-ice concentration above 50% is treated as ice grid. Tests on the sea-ice cutoff threshold are considered in an ongoing study to assess the sensitivity of the data availability to the percentage of sea ice concentration.

Satellite sensors can drift due to several factors, with the sources being physical, geometrical, mechanical, mapping, environmental, random, etc. Satellite orbital drift, sensor degradation, sensor offsets, and signal interference are the common causes of long-term drifts and often lead to bias in the retrievals. For the SSM/I sensor series, the instruments were originally designed for weather and environmental applications and their long-term performance stability has not been thoroughly assessed to date. Therefore, different SSM/I sensors have to be carefully calibrated to a reference satellite or a stable reference system before used in the synthesis. For the OAF flux project, an in situ validation database consisting of 126 buoy time series was established to provide a ground truth for checking potential drifts in input data sets [Yu and Jin, 2012]. Interested readers are referred to Yu and Jin [2012] for the list of buoy locations and detailed discussions of the buoy-based statistical evaluation of the 12 input data sets in the OAF flux analysis. Mean drifts were identified mostly in the SSM/I sensors (e.g., F14, F15, and F16); they were truncated to prevent potential bias effect on the synthesis. The actual data periods used in the OAF flux synthesis are shown in Figure 1b.

2.3. Atmospheric Reanalysis Winds

Two atmospheric surface wind reanalyses are used as the background data during the OAF flux synthesis. One is the European Centre for Medium-Range Weather Forecasts (ECMWF) Re-Analysis (ERA) interim (hereafter ERA-Interim) project [Dee *et al.*, 2011] and the other is the Climate Forecast System Reanalysis (CFSR) from the National Centers for Environmental Prediction (NCEP) [Saha *et al.*, 2010]. ERA-Interim is the latest global atmospheric reanalysis produced by ECMWF that covers the period from 1979 onward. Wind vectors at 10 m height are available at approximately 0.7° spatial resolution and six-hourly temporal resolution. CFSR is the third generation reanalysis product by NCEP. It is a global, high-resolution, coupled atmosphere-ocean-land surface-sea ice system, with surface winds at 10 m height available every hour at roughly 0.3° spatial resolution. It is worth noting that both reanalyses included substantial satellite vector wind observations in the data assimilation of surface winds. The three scatterometers, ERS-1, ERS-2, and QuikSCAT, were used in both assimilation systems. Additionally, ERA-Interim utilized ASCAT starting from March 2008 [Poli *et al.*, 2010], whereas CFSR assimilated WindSat from September 2008 [Saha *et al.*, 2010].

To be consistent with the format of satellite wind retrievals, the winds from the reanalyses were adjusted to the height of 10 m equivalent neutral winds following *Liu and Tang* [1996].

3. Rationale Supporting the Synergy Between Scatterometers and Radiometers

3.1. A Theoretical Perspective

At microwave frequencies, the backscatter of the ocean surface is related to the spectral density of the capillary-gravity waves. The growth of these waves is strongly correlated with the surface winds, and the correlation establishes the theoretical basis of scatterometry [*Brown*, 1979]. A radiometer measures the sea surface microwave emissions, and the strength of the brightness temperature shows a strong sensitivity to surface roughness created by wind forcing. The two instruments use different electromagnetic properties to retrieve ocean surface winds, but both retrieve winds from ocean surface short-scale waves (i.e., gravity-capillary and capillary surface waves with wavelengths in the range of a millimeter to several centimeters) that constitute surface roughness.

The so-called two-scale scattering approximation [*Phillips*, 1957] is the most widely accepted theoretical model of the scattering and emission from the ocean surface [*Wentz*, 1975; *Brown*, 1979; *Plant*, 1986; *Donelan and Pierson*, 1987; *Yueh et al.*, 1994; *Lemaire et al.*, 1999]. The basic idea of the two-scale model is to divide the surface wave spectrum into two parts: one corresponds to the Kirchhoff regime for the large-scale component that can be approximated as specular reflection, and the other corresponds to the Bragg regime for the small-scale component with modulation from tilts of large-scale waves. For satellite scatterometry, the primary mechanism for backscattering radar pulses is the Bragg resonance, and the secondary mechanism is the longer wave modification of local incidence angle through tilting the Bragg resonance surface roughness. For satellite radiometry, the two modes of waves together with sea foam—the latter becomes important for wind speeds above 8 m s^{-1} —are three important types of roughness scales that contribute to ocean surface emissivity [*Meissner and Wentz*, 2012]. These roughness contributions to the surface emissivity can be approximated as integral functions of the product of electromagnetic weighting functions and the surface roughness spectrum [*Yueh et al.*, 1994; *Wentz*, 1997]. The weighting functions have resonance peaks when the surface wavelength scale is comparable to the electromagnetic wavelength. In this regard, both active and passive remote sensing problems depend on the roughness properties of small-scale wave components in the vicinity of Bragg resonance [*Donelan and Pierson*, 1987; *Yueh et al.*, 1994, 1995].

In analyzing coincident measurements with a 37 GHz polarimetric radiometer and a 10 GHz scatterometer from an aircraft field experiment conducted in 1995, *Weissman et al.* [2002] showed that both scatterometer and radiometer in study respond to short sea surface waves of very similar wavelengths and have similar sensitivity to wind speed (or friction velocity) and direction. Their analysis provided supporting evidence that the azimuthal signatures of the two instruments are from the same geophysical process: the angular dependence of short waves on the ocean surface and the tilting of the local incidence angle by the longer waves. On the other hand, their analysis also revealed that the two instruments have different dependences on the incidence angle with respect to the longer wave tilting effect. While the intensity of the brightness temperature increases with the increasing incidence angle [*Yueh et al.*, 1995], the strength of scatterometer normalized radar cross section (σ_0) decreases with the increasing incidence angle [*Schroeder et al.*, 1985]. The opposite dependence of the two sensors on the incidence angle becomes more apparent at low incidence angles and high wind speeds [*Plant et al.*, 1999; *Freilich and Vanhoff*, 2003]. SSM/I measurements are made at a nominal incidence angle of 51° , while scatterometer measurements are obtained from a range of incidence angles.

For moderate wind conditions, the correlation between radar backscatter and vector wind is strong [*Donelan and Pierson*, 1987], and wind retrievals are generally better retrieved. In the low-wind regime, however, airborne-based field observations suggested the existence of a minimum wind speed under which the detected radar backscatter may not be due to wind. *Donelan and Pierson* [1987] explained the observations in terms of the effect of viscosity on the ocean surface that prevents the growth of capillary-gravity waves and creates a cutoff wind speed for scatterometry. They further suggested that the cutoff wind speed is dependent of the sea surface temperature, with a lower cutoff wind speed, usually below 3 m s^{-1} , over the tropical warm waters [*Carswell et al.*, 1994; *Moller et al.*, 2000].

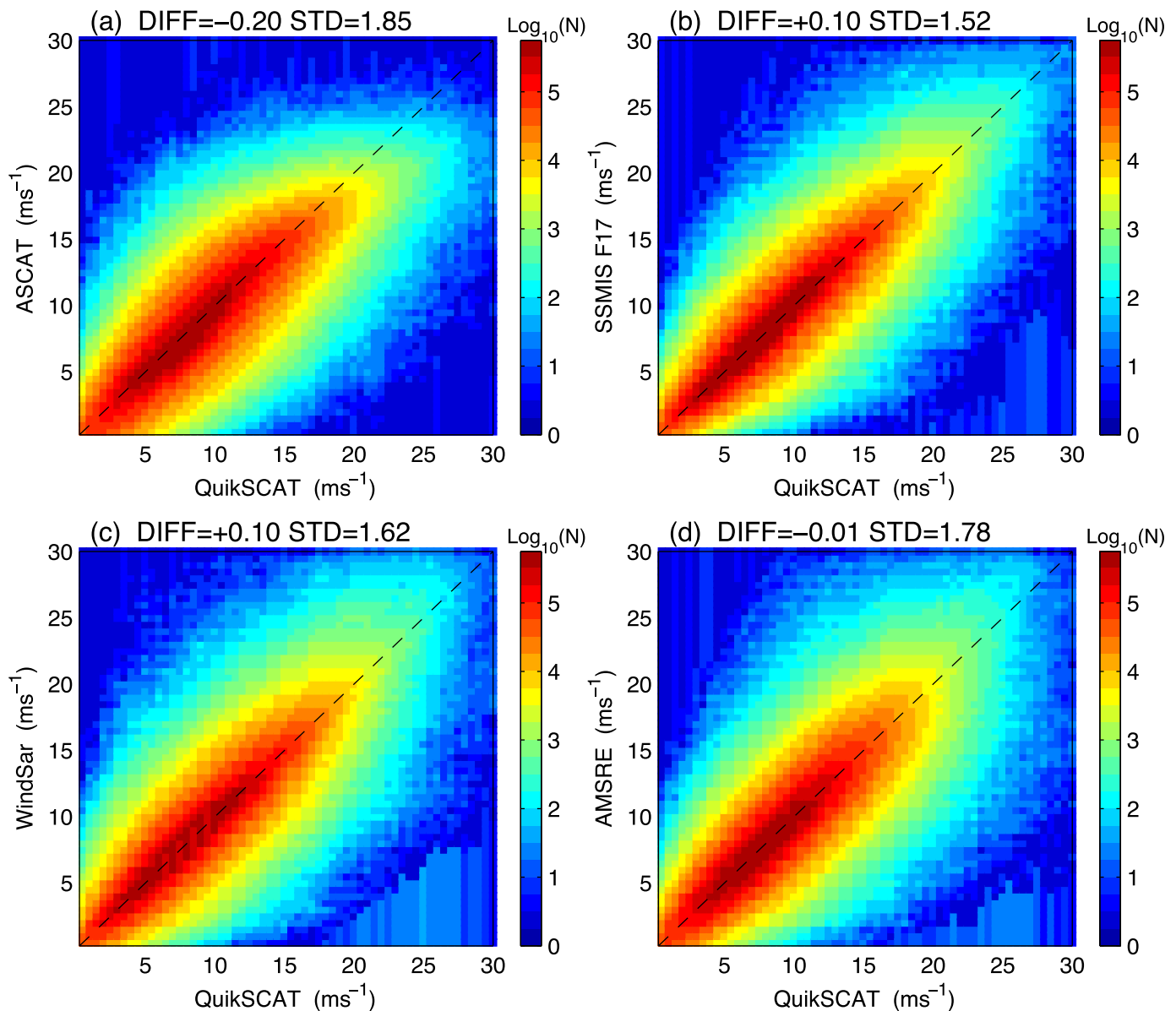


Figure 2. Scatterplots of collocated wind speed pairs in year 2008. (a) ASCAT versus QuikSCAT, (b) SSMIS F17 versus QuikSCAT, (c) WindSat versus QuikSCAT, and (d) AMSRE versus QuikSCAT. A total of 71,965,821 collocation pairs used in each subplot. The mean difference (DIF) and standard deviations (SD) of the difference for each product with respect to QuikSCAT are shown at the top of the frame.

3.2. Evidence From Active and Passive Sensor Retrievals

The compatibility between active and passive remote sensing of ocean surface winds are examined by using wind retrievals from two scatterometers (QuikSCAT and ASCAT) and three radiometers (SSMIS F17, AMSRE, and WindSAT). Figure 2 shows the scatterplots of daily collocations of QuikSCAT with respect to each of the other four sensors for the year 2008. Since all source products were gridded onto the same 0.25° grids, the collocation here represents the availability of daily means from all five products at the grid point. For each product, daily means were computed only for those grid points that have both ascending and descending samples. Collocated wind speeds were then binned into 1 m s⁻¹ bins and plotted with QuikSCAT on x axis and each of the four other sensors on the y axis for wind speeds ranging from 0 to 30 m s⁻¹. In this study, we define wind speeds less than 5 m s⁻¹ as low winds, between 5 and 15 m s⁻¹ as moderate winds, and greater than 15 m s⁻¹ as high winds. Rain-contaminated retrievals have all been discarded. Figure 2a shows that ASCAT agrees well with QuikSCAT up to 15 m s⁻¹. Beyond that range, ASCAT

is weaker than QuikSCAT, with magnitude of the differences increasing with increasing wind speed. The interscatterometer difference at high winds is consistent with existing literature [e.g., *Bentamy et al.*, 2012; *Yu and Jin*, 2012]. Scatterometer retrievals at high winds are an ongoing research subject. Currently, there are no in situ observations to validate the fidelity of these two scatterometers at high winds.

Compared to ASCAT, the three radiometers show a near-linear relationship with QuikSCAT up to 20 m s^{-1} ; beyond that, radiometers are higher than QuikSCAT, particularly evident for WindSat and AMSRE (Figures 2b–2d). It should be noted that QuikSCAT and the radiometers from RSS are intercalibrated. SSMIS F17 appears to have the best consistency with QuikSCAT for the range of wind speeds ($0\text{--}30 \text{ m s}^{-1}$) under examination. In light of the discussion in the above section, radiometers and scatterometers have similar sensitivity to wind speed and direction because they respond to similar short-scale wavelengths. The consistency between the two types of sensors is evidenced in the low and moderate wind speed range, but not as good at high winds. The latter appears to be explainable from the theoretical viewpoint that the two types of sensors have opposite dependences on the incidence angle at high wind speeds—yet, we caution that this may not be the only explanation. The lack of reliable high wind speed ground truth to calibrate the high-wind Geophysical Model Functions (GMFs) as well as a less pronounced dependence of the normalized radar cross section (σ_0) on wind speed at high winds could be a significant contributor to the uncertainty of high wind retrievals [e.g., *Yueh et al.*, 2001; *Fangohr and Kent*, 2012].

Despite the uncertainty concern for the wind retrievals in the low wind speed regime, Figures 2a–2d show no obvious inconsistency between the five products for wind speeds below 5 m s^{-1} . The good agreement between the products could be attributed to two factors. One is that the near-surface wind measurements provided by the global tropical moored buoy array are a reliable ground truth for calibrating and validating the GMFs under low-wind conditions. This appears to be supported by the findings of *Fangohr and Kent* [2012], who evaluated four QuikSCAT products generated from different GMFs and found that systematic differences between products tend to be small, of order 0.1 m s^{-1} and between 3 and 20 m s^{-1} , but for high wind speeds exceeding 20 m s^{-1} , the average absolute differences can be of 10 m s^{-1} . The second factor is that, except for ASCAT, all the other satellite data sets were generated by RSS. The QuikSCAT version 4.0 was processed using a new GMF, Ku-2011, which was developed using wind speed data from WindSat sensor with CCMP winds [*Atlas et al.*, 2011] for direction [*Ricciardulli and Wentz*, 2011]. Meanwhile, all the radiometer sensors were processed from the same radiative transfer models (RTM) version 7.0 [*Wentz*, 2013]. The intersensor consistency between RSS products is ensured.

3.3. Global Wind Distribution in Low, Moderate, and High Wind Categories

The interscatterometer differences at high winds raised such questions as how often and where high winds occur. Answers to these questions will help to assess the degree of potential impacts of intersensor differences at high winds on the multisensor synthesis. The regions that are most frequented by high winds is shown in Figure 3, which is a plot of the total high-wind days for an average year constructed over the 25 year period (1988–2012) from the available eight SSM/I and SSMIS sensors. Evidently, most high wind events occur at latitudes of westerly winds between 30° and 60° in both hemispheres. The maximum occurrence is associated with the southern hemisphere westerly wind belt, where the total number of high wind days exceeds 40 days per year in most areas and up to 65 days in the Indian Ocean sector. The second maximum occurrence is in the subpolar North Atlantic Ocean basin, where on average there are about 40–50 days of high-wind events each year. Almost all the high winds occur during the respective hemisphere's fall/winter seasons.

The percentage of the global distribution of high winds was computed by grouping the wind at 0.25° grids into the three wind speed categories: low, moderate, and high winds. The SSM/I and SSMIS wind speed observations during the 1988–2012 period were used for computation. It is obtained that, on an annual basis, high winds account for only 2.2% over the global field, while low winds and moderate winds contribute to 20.2% and 77.6%, respectively. This shows that 98% of the global daily wind fields are subject to low and moderate winds, with high winds contributing to a mere 2%. Low and moderate winds are the range of wind retrievals that scatterometer and radiometer products have the best agreement and best quality. The compatibility between all input satellite products for wind speeds below 15 m s^{-1} and the 98% dominance of the low and moderate winds on the global scale establishes a solid base that wind retrievals from the two different types of sensors can be integrated.

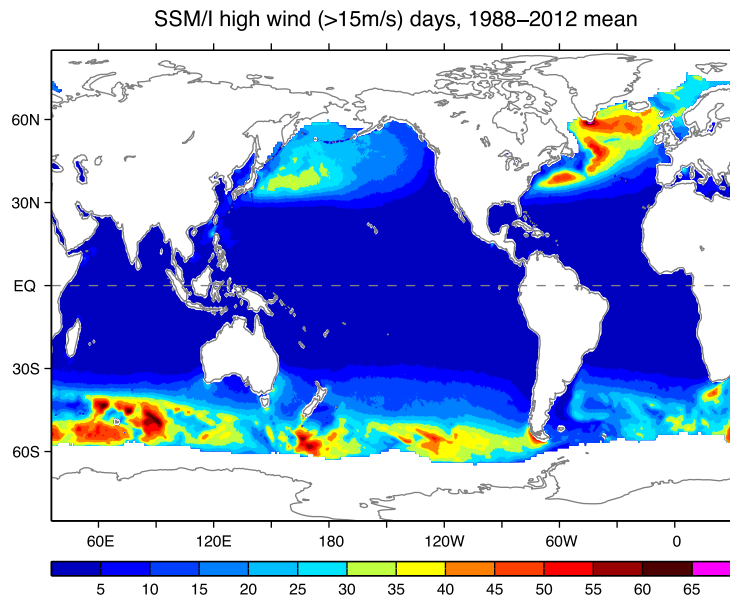


Figure 3. Global distribution of the number of days that wind speeds exceed $15 \text{ m s}^{-1}/\text{yr}$ constructed from SSM/I and SSMIS sensors during the 25 year (1988–2012) period. The high winds account for roughly 2% of global daily wind fields.

4. Methodology and Strategy of Synthesis

4.1. Methodology

The methodology of the OAF flux objective synthesis is based on the theory of the least-variance linear statistical estimation [Daley, 1991; Talagrand, 1997]. It allows the formulation of a least squares estimator (the so-called cost function) to include not only data from different sources but also a priori information that one wishes to impose to constrain the solution. The approach has been used to produce the OAF flux analysis of global ocean evaporation, latent and sensible heat fluxes [Yu, 2007; Yu and Weller, 2007; Yu et al., 2008]. In developing the OAF flux ocean surface vector wind analysis, a major technical challenge was to derive the directional information that is consistent with the SSM/I wind speed retrievals for the pre-QuikSCAT years when there were no scatterometer input data sources (Figure 1). Our strategy was to utilize the surface vector wind fields from atmospheric reanalysis as the first guess for zonal (u) and meridional (v) wind components, and adjust u and v iteratively by imposing two types of constraints. One is that (i) the analyzed wind speed $w = \sqrt{u^2 + v^2}$ should be as close as possible to satellite wind speed retrievals in a least squares sense, and the other is that (ii) the solution of (u, v) should satisfy a set of kinematic constraints such as vorticity and divergence conservations. The addition of vorticity constraints on wind vectors was first developed by Hoffman [1984] to remove the ambiguity of the Seasate-A Satellite Scatterometer (SASS) winds. It was also employed by Legler et al. [1989], Stoffelen and Anderson [1997], Hoffman et al. [2003], and Atlas et al. [1996, 2011] in their studies.

Under these considerations, the cost function formulated for the OAF flux synthesis, F , can be expressed as follows:

$$F = \underbrace{\frac{1}{2}(\vec{V}_a - \vec{V}_b)^T R_b (\vec{V}_a - \vec{V}_b)}_{(i)} + \underbrace{\frac{1}{2}(\vec{V}_a - \vec{V}_o)^T R_o (\vec{V}_a - \vec{V}_o)}_{(ii)} + \underbrace{\frac{1}{2}(w_a - w_o)^T S_o (w_a - w_o)}_{(iii)} + \dots \tag{1}$$

$$+ \underbrace{\gamma(\nabla \times \vec{V}_a - \nabla \times \vec{V}_b)^2}_{(iv)} + \underbrace{\lambda(\nabla \vec{V}_a - \nabla \vec{V}_b)^2}_{(v)}$$

where $\vec{V} = (u, v)$ is the wind vector with the zonal and meridional wind components denoted as u and v , respectively, and $w = \sqrt{u^2 + v^2}$ is wind speed. The superscript “ T ” denotes transpose. There are three subscripts: “ a ” denotes an estimate, “ b ” the background information, and “ o ” satellite observations. The matrices R_b , R_o , and S_o are weighting matrices that, theoretically, are inversely proportional to the respective error covariance matrices of the background wind vector fields (\vec{V}_b), satellite wind vector observations (\vec{V}_o), and satellite wind speed observations (w_o). The parameters, γ and λ , are the scalings.

There are five terms on the right-hand side of the cost function (1). The first three terms (I)–(III) are data constraints that represent a least squares fitting of the analyzed zonal wind, meridional wind, and wind speed to input background and satellite data sets. ERA-Interim and CFSR supply the background information that is needed for two occasions: (i) initialization of wind direction when there are no scatterometer measurements prior to 1999, and (ii) gap-filling of missing values in satellite observations. The fourth and fifth terms, (IV) and (V), are weak constraints based on the vorticity and divergence of ERA-Interim and CFSR, and the contribution of these kinematic terms to the minimization process is set to be small by prescribing the scaling parameters γ and λ . The minimization process seeks an optimal estimate of daily wind field that satisfies the data constraints (i.e., terms (I)–(III) in equation (1)) within the specified weight matrices for the given sets of weak constraints (i.e., terms (IV) and (V)). A conjugate-gradient method was used for the optimization and the process was similar to the one applied in constructing the OAFflux latent and sensible heat fluxes [Yu *et al.*, 2008].

4.2. Weight Assignment

The weight associated with each term in the cost function (1) is inversely proportional to the error covariance matrix of the input data field. Error statistics for each input data set are needed to determine the weights, but none of input satellite and reanalysis data sources provides error estimates for wind speed/direction. Weights determine the goodness of fit between analyzed variable fields and input data fields. If an input data set has large uncertainty, the contribution of input data to the cost function is small, and vice versa. The lack of error information for the input data sets limits our ability to prescribe “true” weights for the terms in the cost function (1). In light of the situation, we resorted to in situ air-sea buoys to guide the weight assignments based on the buoy evaluation of input satellite data sets. It is worth noting that buoy winds are the independent validation reference for the OAFflux analysis; they are not included in the cost formulation (1). The buoy-based statistical evaluation was established from 126 buoy time series, 106 of which were from the tropical moored array system [Yu and Jin, 2012] where wind speeds are generally less than 15 m s^{-1} . This indicates that the buoy evaluation may be sufficient to characterize the error statistics of the low and moderate winds that account for 98% of the global daily wind fields, but it has limitation to provide relevant reference for high winds.

For simplicity, we assume that the weights are constant and the cost function (1) can be simplified as follows:

$$F = \underbrace{\frac{1}{2} \sum_{i=1}^I \alpha_i (u_a - u_i)^2}_{(I)} + \underbrace{\frac{1}{2} \sum_{i=1}^I \alpha_i (v_a - v_i)^2}_{(II)} + \underbrace{\frac{1}{2} \sum_{j=1}^J \beta_j (w_a - w_j)^2}_{(III)} + \dots + \underbrace{\gamma (\nabla \times \vec{V}_a - \nabla \times \vec{V}_b)^2}_{(IV)} + \underbrace{\lambda (\nabla \cdot \vec{V}_a - \nabla \cdot \vec{V}_b)^2}_{(V)} \quad (2)$$

where α_i represents the weight assignment for zonal and meridional wind components, with the subscript $i = 1, \dots, I$ indicating the respective input satellite (i.e., QuikSCAT and ASCAT) plus background (i.e., ERA-Interim and CFSR) data sets for wind components. The weight assignment for the wind speed term is denoted by β_j , with the subscript $J = 1, \dots, J$ indicating the respective input satellite wind speed data sets (e.g., SSM/I F08, F10, F11, F13, F15, SSMIS F16, F17, AMSRE, WindSat, QuikSCAT, and ASCAT). The weights, β_j , associated with the wind speed constraint (term (III)), were set to be 1. For the period when only one scatterometer is available, the weight associated with the scatterometer-derived u and v constraints (terms (I) and (II)) was taken as the sum of the number of available wind speed data sets, i.e., scatterometers and radiometers included. The weights of the ERA-Interim u and v terms were assigned to be 0.8, and the scaling parameters of the kinematic constraints for vorticity and divergence, γ and λ , were fixed at 0.5. The values of the scaling parameters were based on numerous sensitivity experiments we have conducted. As the weights are assigned, the sensitivity of the optimal solution to a range of weight assignments was examined, and the resulting uncertainty estimation of the synthesis was derived.

5. Challenging Issues for the Multisensor Synthesis

5.1. Selection of Spatial and Temporal Resolution

The 25 km resolution is a nominal resolution used in processing all satellite wind retrievals and is the spatial resolution of the OAFflux synthesis. However, the selection of the temporal resolution is a trade-off between the minimization requirements of solving equation (1) and data coverage from available sensors. The solution of equation (1) is the best fit when there are sufficient observations such that the random errors in the

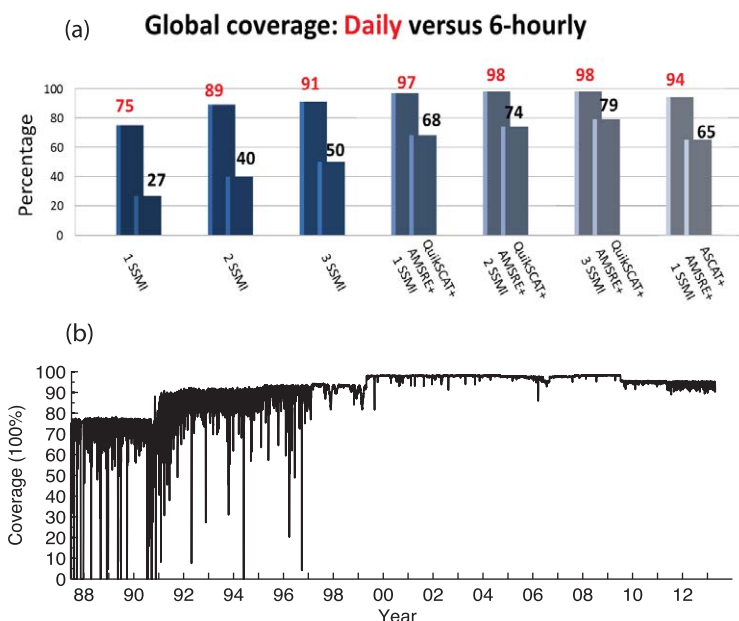


Figure 4. (a) Percentage of the global six hourly (numbers in black) and daily coverage (numbers in red) for the types of sensor combination occurred during the OAFflux analysis period. (b) Percentage of the global daily coverage based on all available sensors.

data are reduced and the error variance is minimized. During the 25 year analysis period, the number of available sensors varies with time (Figure 1). The time series starts with one sensor in July 1987, followed by a two or three-sensor constellation over most of the 1990s, and expanding up to a maximum of the seven-sensor constellation in the mid-2000s. Figure 4a shows the global coverage for two temporal resolutions, six hourly and daily, based on the sensor combinations that occurred during the analysis period. Removal of rain contamination reduces the total number of wind retrievals by 2–10% depending on the sensor type. Figure 4a suggests that, if a six-hourly resolution is used, the percentage of global coverage changes from 27%, when only one SSM/I is available, to a maximum of 79%, when QuikSCAT and four radiometers (AMSRE and 3 SSM/I sensors) are available. On the other hand, if a daily resolution is chosen, the minimum coverage is 75% for the first few years when there is only one SSM/I sensor and is near global (~98%) during the QuikSCAT period (1999–2009). After November 2009, a combination of ASCAT with SSMIS provides up to 94% of global coverage. The difference in daily coverage between using ASCAT instead of QuikSCAT is due to ASCAT swath configuration that yields an average 70% of daily coverage over the global ocean. It should be noted that a full 100% coverage is not likely because of rain. The Ku-band QuikSCAT is sensitive to heavy rains, while passive radiometers have no observations under all rain conditions. The C-band ASCAT is less sensitive to direct rain effects [Portabella et al., 2012], but the daily coverage at 70% is not sufficient to cover all the rain areas where radiometers have no observations.

From a least squares perspective, if the number of observations over the global grid points is less than the number of grid points, the minimization problem is underestimated and has infinite solutions (or no unique solution). In this case, one needs to rely on the background data set (such as the reanalysis) to select a solution, which makes the estimated vector wind fields at the solution lean heavily toward the background information for the regions that have no satellite observations. If the background data sets have a coarser spatial resolution and a smoother pattern, they would show up in the estimated wind fields and cause an uneven distributed spatial structure, resulting in finer-scale spatial variability in the regions covered by satellites and a smooth structure in the regions of no satellite data. Hence, we selected a daily resolution for the OAFflux product to ensure a maximum global coverage.

5.2. Data Gap Filling

Missing data over the open ocean are caused mainly by two factors: interswath gaps between ascending and descending passes and the elimination of rain-contaminated wind vector cells. In some cases, shut-down of satellite instrument when an anomaly is detected on the spacecraft can cause the loss of satellite

observations for an extended period of time. The impact of instrument shutdown is felt more sharply before 1997 (Figures 1a and 1b) when there were only 1–2 sensors available. Wind fields from numerical weather prediction models are resorted upon when satellite observations are lacking, which is used in most practices to provide complete daily maps. For instance, the six-hourly cross-calibrated multiplatform (CCMP) ocean surface wind product [Atlas *et al.*, 2011] applied the 40 year ECMWF Re-Analysis (ERA40) and operational analysis to fill in sampling gaps. For the OAFlex synthesis, the model winds used as the background information were the six-hourly 0.7° gridded ERA-Interim winds [Dee *et al.*, 2011].

Atmospheric reanalyzed winds are not satellite winds although satellite winds are assimilated in the models. To use ERA-Interim winds for gap filling due to swath gap and rain, the differences between the ERA-Interim and satellite need to be mitigated. The approach we implemented is described in Figures 7a–7f using the synthesis on 1 January 1990 as an example. There was one passive microwave radiometer (i.e., SSM/I F08) available at that time and so the effect of the gap filling on the final solution can be seen more clearly. Each SSM/I sensor has two time files per day (ascending and descending passes), marked by Coordinated Universal Time (UTC) in tenths of hours. Each time file represents the corresponding time of the swath sample used to interpolate the given grid cell for either ascending or descending orbits. Although the OAFlex synthesis was conducted on a daily mean basis, the gap filling was performed for each satellite pass using the six-hourly ERA-Interim at the nearest time. By doing so, short-term variability (such as isolated short-lived storms, fast-moving synoptic systems, diurnal rainfall variability, etc.) can be better represented instead of being smoothed out by daily means.

Illustration of the gap-filling approach is provided in Figures 5a–5e using the 1 January 1990 as an example. The gaps between overpass swaths (Figures 5a–5b) together with the loss of observations under rain lead to missing data over a considerable spatial extent. The first step of gap filling was to match the ERA-Interim 6 h intervals (Figures 5c and 5d) with the nearest observing time associated with the ascending and descending passes (Figures 5a and 5b). The next step was to use the selected reanalysis 6 h products to fill in SSM/I gaps. Satellite winds are known to be higher than winds from global reanalysis models both in the mean and for extreme cases [Brown, 2002; Yu and Jin, 2012]. An adjustment was made to ERA-Interim using a 3 day mean satellite field for wind speed fields. This approach was developed from the fact that one single SSM/I (or SSMIS) sensor can provide a complete global coverage in 3 days. The 3 day mean difference between SSM/I and ERA-Interim was the base reference when adjusting the magnitude of the ERA-Interim wind speed. Zonal and meridional wind components are also scalars, but the cancellation between positive and negative signs complicates the meaning of the 3 day mean. The gap-filling approach was not applied to the wind component fields. The final synthesized wind speed field is shown in Figure 7e.

5.3. Sensitivity of the Daily Mean Field to High Winds and Rain

The most challenging situation for the multisensor synthesis is the construction of the daily mean fields associated with high-wind, heavy-rain storm systems. Passive microwave radiometers have no observations under rain conditions, while the C-band ASCAT and the Ku-band QuikSCAT have different responses to rain, causing persistent interscatterometer differences in high winds over the overlapping areas [Weissman *et al.*, 2012]. One case analysis is presented in Figures 6a–6f, in which satellite wind observations of Hurricane Bill on 22 August 2009 from four sensors are examined. On that day, the storm was located in the northwest Atlantic, and satellite wind observations of the system include wind speed and direction retrievals from ASCAT and QuikSCAT and also wind speed retrievals from AMSRE and SSMIS F17. WindSat, SSM/I F13, and SSMIS F17 were also available at that time and were used in producing the OAFlex synthesis. But for simplicity, the three sensors were not presented here, as the three radiometers have similar characteristics to those of AMSRE and SSM/I F17. Their role in the synthesis is to increase the number of samplings over the rain-free regions, which helps to optimize the solution, but the impact on reconstructing the near-surface wind pattern associated with rain is limited because they provide no observations in rainy areas.

Figures 6a–6d show the daily coverage of the Atlantic region of interest (10°N – 60°N , 85°W – 20°W), produced by overlaying the ascending and descending passes for each of the four sensors. Evidently, the ASCAT's two swaths leave large areas between swaths unsampled. Nevertheless, the C-band sensor has a clear advantage of being less susceptible to rain and hence more capable of capturing the storm's near-surface wind field if the storm's location happens to fall within the orbit passes (Figure 6a). On the other hand, rain has a larger effect on attenuating and scattering the radar energy at Ku-band (13.4 GHz) [Sobieski *et al.*, 1999; Draper and Long, 2004], so that QuikSCAT cannot "see" through heavy rain. As is seen from

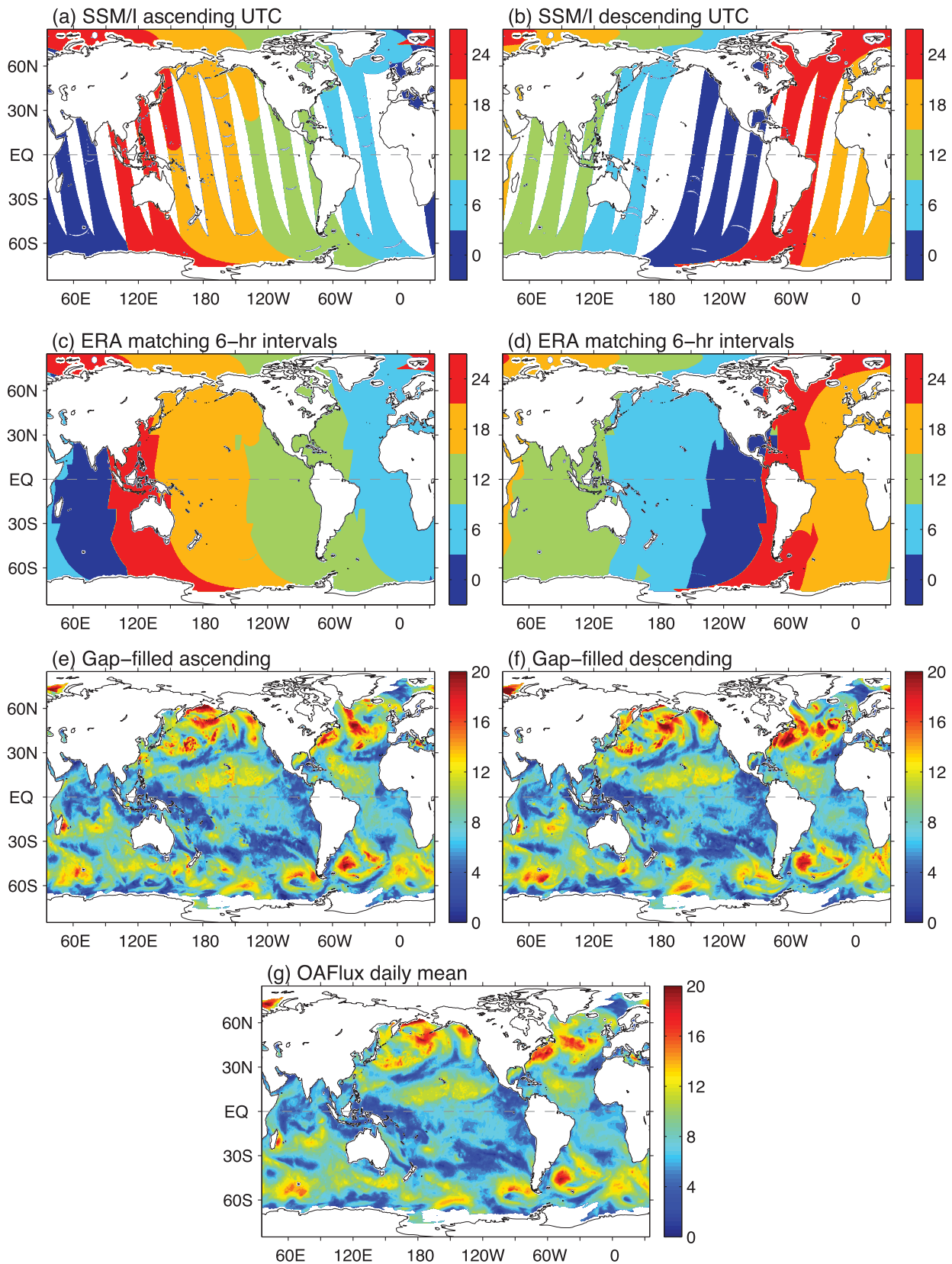


Figure 5. Illustration of the gap-filling approach on the 1 January 1990. (a, b) The SSM/I observing time in UTC for the respective ascending and descending passes. (c and d) The nearest ERA-Interim 6 h intervals that are used to fill in the gaps in the two SSM/I passes. (e) The daily mean field produced from the OAFlex daily synthesis.

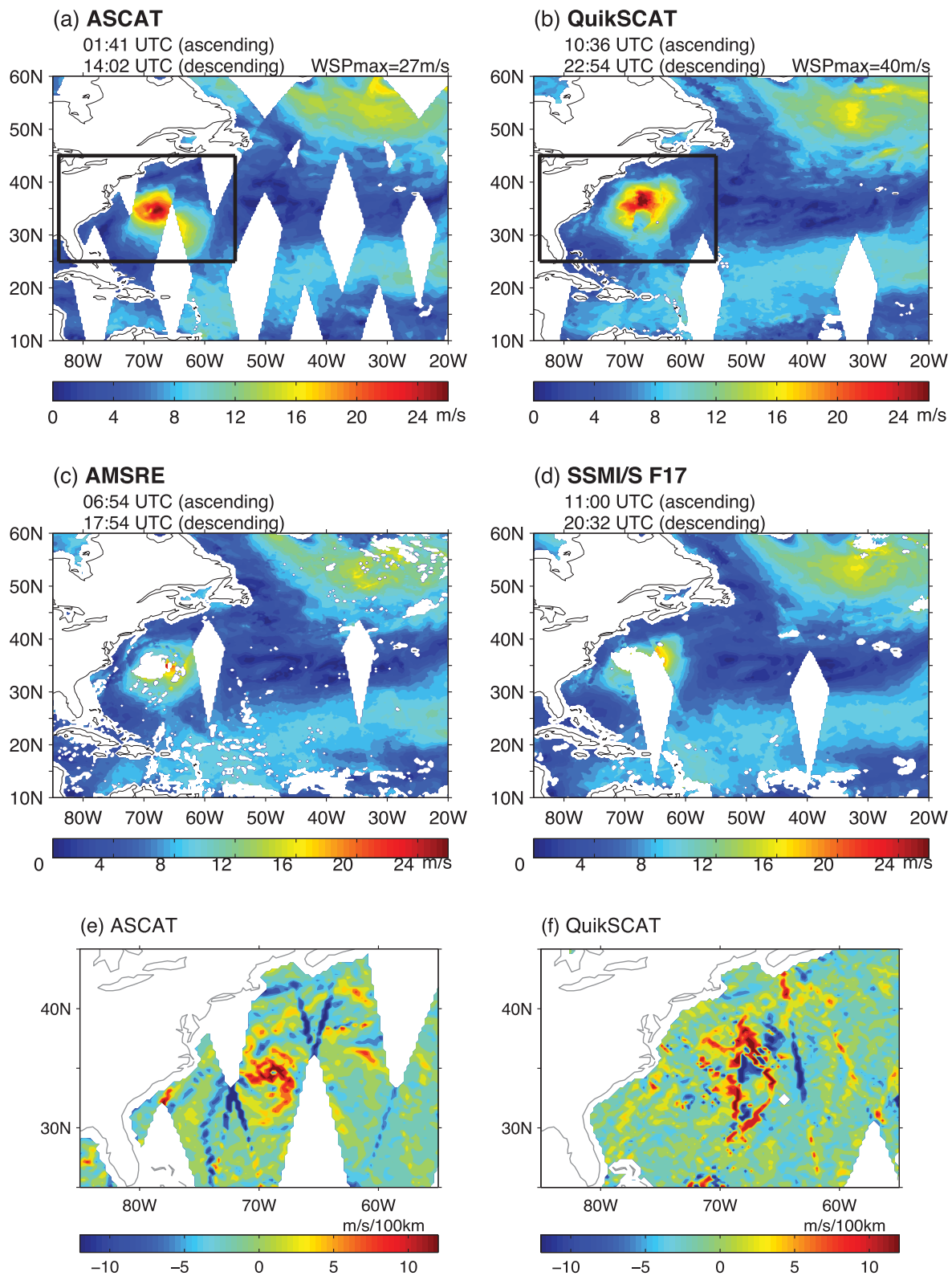


Figure 6. Wind speed retrievals on 22 August 2009, the day when Hurricane Bill moved to the northwest Atlantic. Daily coverage from combining ascending and descending passes is shown for (a) ASCAT, (b) QuikSCAT, (c) AMSR-E, and (d) SSMIS F17. The square boxed region in Figures 6a and 6b is closed up for examining wind convergence ($\partial u/\partial x + \partial v/\partial y$) constructed from (e) ASCAT and (f) QuikSCAT. The positive values in Figures 6e and 6f denote convergence and negative values denote divergence.

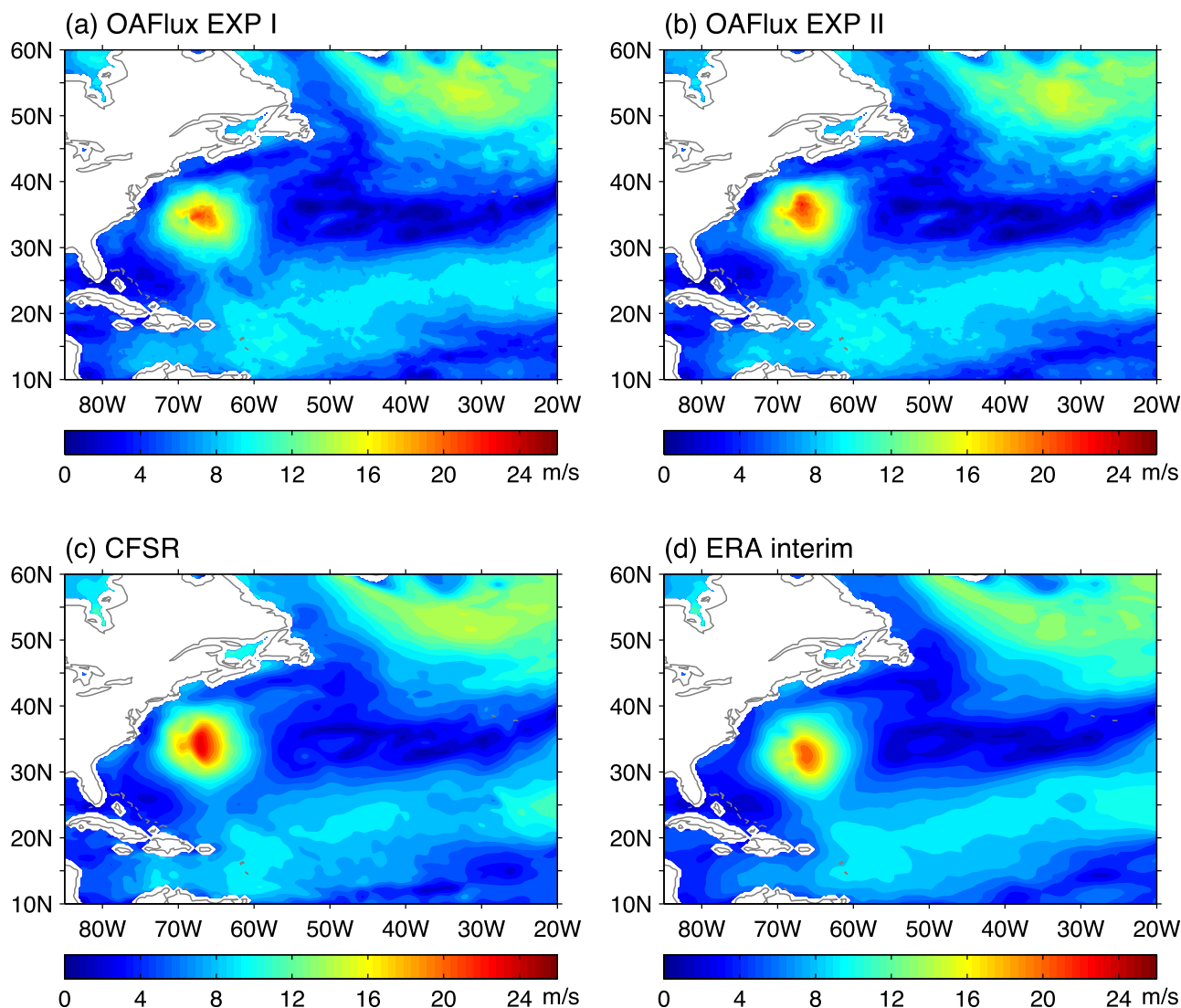


Figure 7. Daily mean wind speed on 22 August 2009 from (a) OAFlex experiment I using ASCAT, SSMIS F17, and AMSRE; (b) OAFlex experiment II using QuikSCAT, SSMIS F17, and AMSRE; (c) CFSR; and (d) ERA-Interim. The two OAFlex experiments tested the effect of interscatterometer differences in constructing the daily mean surface wind field. The daily mean fields from CFSR and ERA-Interim were constructed from the respective hourly and six-hourly outputs.

Figure 8b, a sizable portion of high winds near the storm center is smeared after rain-contaminated wind vector cells (WVCs; or latitude/longitude grid boxes) were removed from QuikSCAT retrievals. The impact of eliminating rain-contaminated QuikSCAT WVCs is seen more clearly from the near-surface wind convergence field ($\partial u/\partial x + \partial v/\partial y$) of the storm (Figures 6e–6f, which are the convergence fields in the boxed area in Figures 6a and 6b). The storm’s eye and the bands of intense surface convection that spiral around the storm’s center are visible in ASCAT, but are distorted significantly in QuikSCAT. Anomalous convergence/divergence lines along the edges of the swaths are shown in both fields, which can be largely attributed to the changes of surface wind synoptic variability between the time lapse of the ascending and descending passes. The two passes represent two time discrete snapshots of satellite observations of surface winds. In case of fast-moving weather systems, it seems that more sensors (or passes) are needed to better represent the variability of the weather system and hence provide a better daily mean.

The OAFlex multisensor synthesis is sensitive to the interscatterometer differences associated with heavy rain storms. To demonstrate the effect, two synthesis experiments were conducted. In experiment I, the synthesis was based on ASCAT and SSMIS F17 and AMSRE, while in experiment II, the synthesis was based on QuikSCAT and the same two radiometers. In both experiments, missing data in wind speed fields were filled

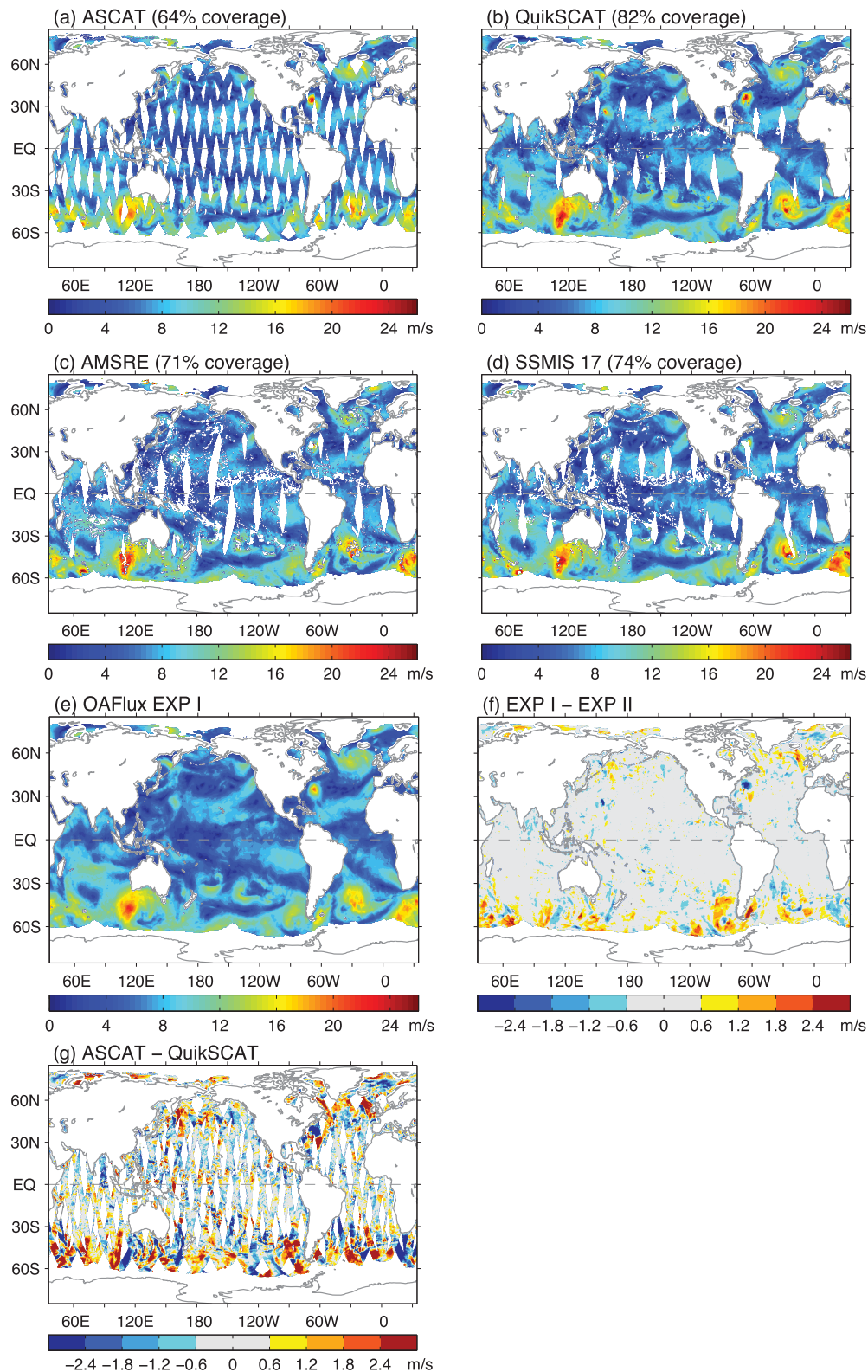


Figure 8. Global daily mean wind speed field on 22 August 2009 from (a) ASCAT, (b) QuikSCAT, (c) AMSRE, and (d) SSMIS constructed from overlaying the ascending and descending passes. (e) OAFIux experiment I using ASCAT, SSMIS F17, and AMSRE; (f) differences of experiment I from experiment II that used QuikSCAT instead of ASCAT; and (g) differences between ASCAT and QuikSCAT.

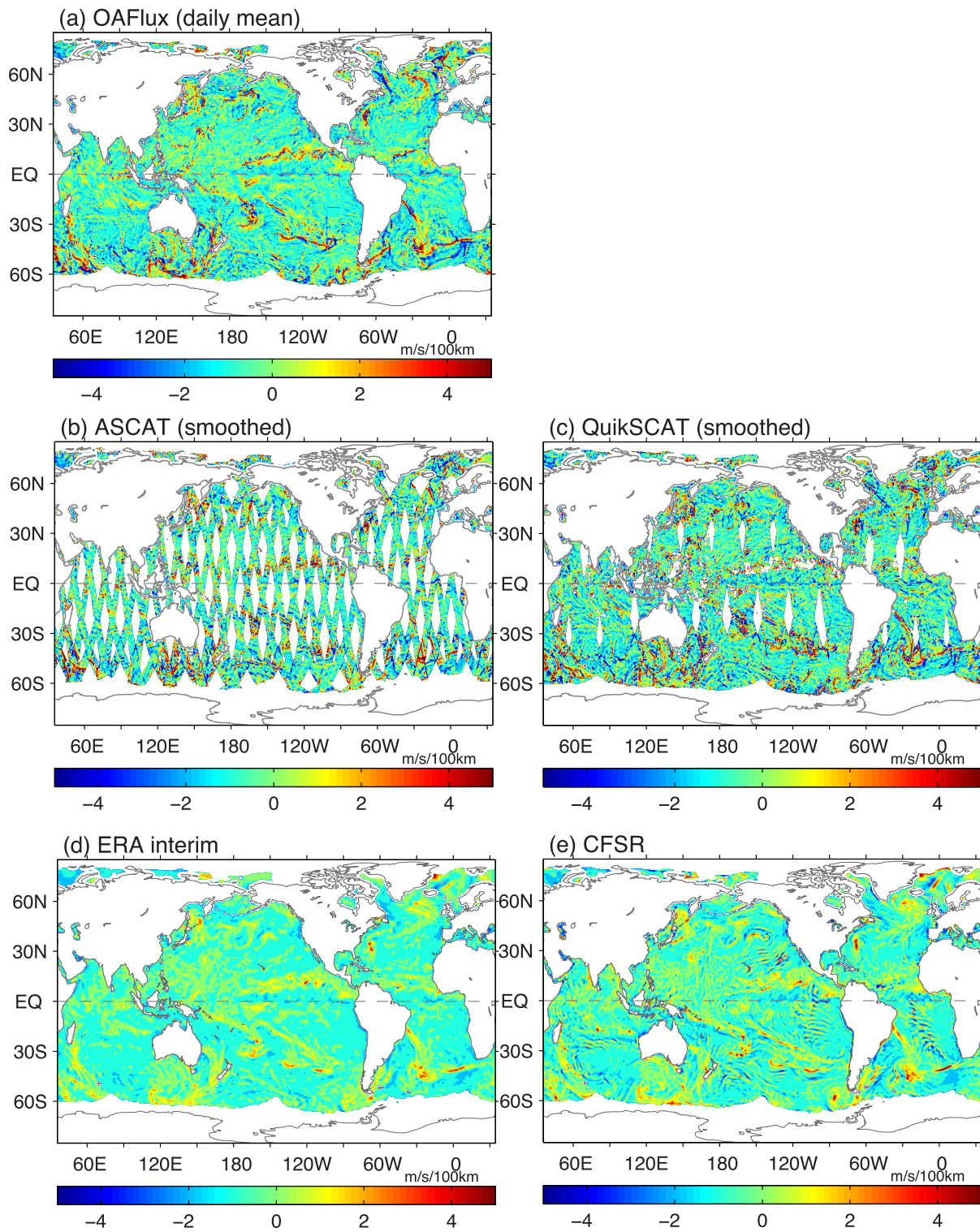


Figure 9. Near-surface wind convergence/divergence on 22 August 2009 constructed from (a) OAFlex, (b) ASCAT, (c) QuikSCAT, (d) ERA-Interim, and (e) CFSR. The two scatterometer fields in Figures 9b and 9c were applied a 1–2–1 spatial filter. Positive values denote convergence and negative values denote divergence.

in with mean-adjusted ERA-Interim surface wind speeds. The wind speed fields from the two experiments are shown in Figures 7a and 7b. The two experiments produced very similar patterns and similar magnitudes over the broad regional scale except for the storm center, where the interscatterometer differences cause the storm's high wind pattern to vary considerably with the experiment. The storm center is more elongated in the QuikSCAT experiment (experiment II) while more rounded in the ASCAT experiment (experiment I).

Depicting the storm center's high winds challenges not only satellite observations but also atmospheric reanalyses. The difficulty for obtaining a consistent pattern of the storm's near-surface wind structure is illustrated in Figures 10c and 10d, in which daily mean wind speed fields from CFSR and ERA-Interim are displayed. The two reanalyses, albeit smooth, have a regional pattern in good agreement with the two sensitivity experiments. However, the shape and magnitude of the high winds around the center of the storm differ substantially. Both reanalyses assimilated QuikSCAT and ERA-Interim included also ASCAT. The lack of consistency between reanalyses underlines the models' deficiencies in capturing synoptic variability of near-surface wind.

The effects of the interscatterometer differences on the global scale are examined in Figures 8a–8g using the same date as above. It is observed that ASCAT alone provides 65% of the global coverage and missing data are due primarily to the gaps between swaths (Figure 8a). QuikSCAT covers 85% of the global oceans, and missing data are attributable to both interswath gaps and heavy rain contamination (Figure 8b). The two radiometers, AMSRE and SSMIS 17 (Figures 8c and 8d), have a global coverage of 68% and 74%, respectively, and the effect of rain on causing data gaps is particularly pronounced along the tropical rain belts of the Intertropical Convergence Zone (ITCZ) and the South Pacific Convergence Zone (SPCZ).

The global wind speed fields produced by the two sensitivity experiments, experiment I (Figure 8e) and experiment II (not shown), have good agreement in spatial details over the global scale but differ in synoptic scales associated with propagating weather events (Figure 8f). Experiment II that used QuikSCAT instead of ASCAT produced stronger high winds for storms. This is seen not only in the Northwest Atlantic where Hurricane Bill was located but also more pungently in the southern midlatitudes between 30°S and 60°S where three intense storms were swirling around, with one located southwest of Australia and the other two in the south Atlantic sector. The wind speed difference field between ASCAT and QuikSCAT retrievals (Figure 8g) shows that, despite an incomplete global coverage, the difference anomalies exceeding 3 m s^{-1} are located primarily in the midlatitude storm track regions (30–60° north and south). Evidently, the synthesis has reduced considerably the difference anomalies between the two sensors, and differences of magnitude larger than 1 m s^{-1} occur mostly at locations of high wind speeds induced by passing storms. This suggests that the inclusion of radiometers in the multisensor synthesis can accommodate most of the differences in the scatterometers, except for high winds and rain conditions.

6. OAFlex Versus Scatterometer and Atmospheric Reanalysis Daily Mean Fields

The meaning of the OAFlex synthesized daily mean winds is different from that of the scatterometer-based daily mean winds. OAFlex constructs the daily mean field from multiple sensors, with the number of passes (descending + ascending) ranging from 2 to 14 per day during the analysis period. On the other hand, the daily mean field of a satellite sensor is the summation of two passes (or snapshots), i.e., ascending and descending passes, for each day. Here the daily mean fields from OAFlex are compared with scatterometers to elucidate the differences between them. Comparison between OAFlex and atmospheric reanalysis daily mean fields is also conducted for two reasons. One is that OAFlex is not independent from ERA-Interim and CFSR, as the latter served as the initialization and the background information for the former. The other reason is that the two reanalyses all assimilated scatterometers ERS-1/2 and QuikSCAT, in addition to ASCAT for ERA-Interim and WindSat for CFSR. The surface winds from the two reanalyses are, in some sense, also satellite-derived products. Hence, there is a need to apprehend the differences between the OAFlex synthesis and the atmospheric reanalysis, and to demonstrate that the surface wind products are so sensitive to the methodology and approaches in use that they differ in spatial details on a daily mean basis. The differences between the products in terms of temporal variability are not discussed in this study, as the issues cover a broad range of topics, with investigation still ongoing.

6.1. OAFlex Versus Scatterometer Daily Mean

Satellite passes are more like "snapshot" views of global fields. The representation of daily mean is affected not only by the global coverage but also by data noise. From a statistical point of view, the errors have

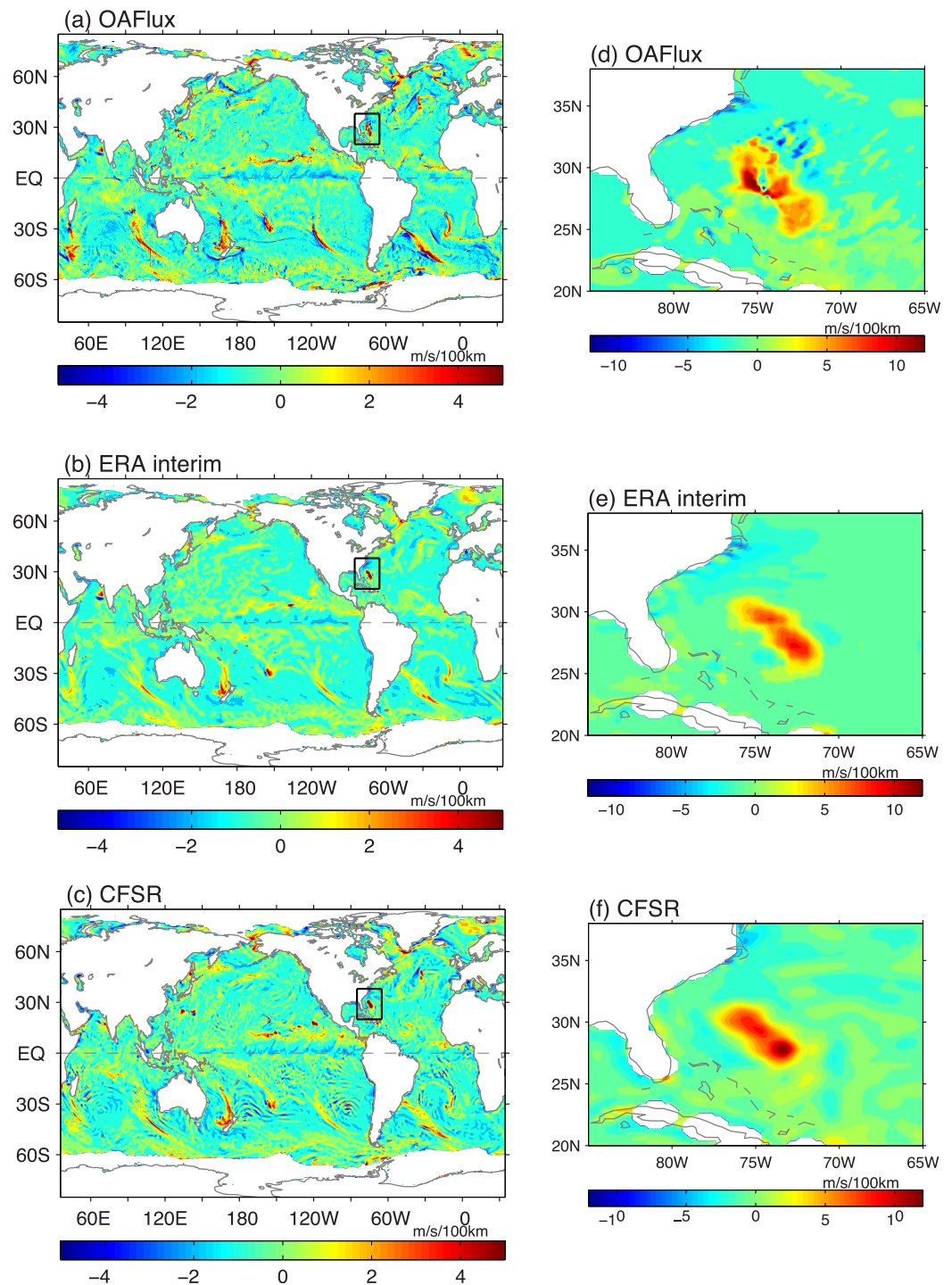


Figure 10. Global near-surface wind convergence/divergence on 25 August 1998 constructed from (a) OAFIux, (b) ERA-Interim, and (c) CFSR. (d–f) The wind convergence associated with Hurricane Bonnie for the corresponding square-boxed region in Figures 10a–10c. Positive values denote convergence and negative values denote divergence.

larger effect on wind derivatives (e.g., wind convergence, vorticity, and wind stress curl) than on winds, because the accuracy of wind derivatives usually reflects the error magnitude in winds. The near-surface wind convergence/divergence over the global ocean constructed from the OAFIux on 22 August 2009 is shown in Figure 9a. The most noted features are the mesoscale convergence/divergence filamentary structures that are present in regions of surface frontal zones, including the Inter-Tropical Convergence Zone

(ITCZ), the South Pacific Convergence Zone (SPCZ), and the midlatitude synoptic weather systems. The fine details of the ITCZ convergence structure in the tropical Pacific around 10°N–15°N latitudes are perceived, showing that the system meanders from the coast of Panama to near the dateline, with segments of strong convergence (denoted by large positive values) filaments embedded along two discrete bands.

The global fields of wind convergence/divergence fields constructed from ASCAT and QuikSCAT on the same day are presented in Figures 9a and 9b, respectively, with a spatial filter applied to both fields. The northwest of the Atlantic of these fields has been used for a close-up of the scatterometer's capability to depict the near-surface circulation associated with Hurricane Bill in section 5.3 (Figures 6e–6f). The global patterns constructed directly from the ASCAT and QuikSCAT derivatives are compounded severely by grid-size noise so that a spatial smoother (1–2–1) was applied to smooth out the grid-size noise to some degree and to uncover useful signals in the fields. After the smoothing, one can clearly identify the marked meso-scale convergence/divergence filamentary structures associated with the ITCZ, the SPCZ, and the midlatitude synoptic weather systems. The filamentary pattern is better seen in the smoothed QuikSCAT field, as it is less interrupted by the diamond-shaped missing data gaps compared to ASCAT.

The comparison between OAF flux and scatterometer daily mean fields shows that the OAF flux synthesis is capable of retaining the key mesoscale front structures in the scatterometer wind derivative fields and meanwhile leaving out the grid-size noises in the satellite retrievals. The reduced noise level in the OAF flux synthesized daily mean field is consistent with the expectation of the least squares approach employed in the OAF flux synthesis, which is to reduce the random errors in the input data and to obtain a solution that has the minimal variance.

6.2. OAF flux Versus Atmospheric Reanalysis Daily Mean

The OAF flux synthesis is not independent of the ERA-Interim and CFSR, as the latter two provide the background information for filling data gaps of the wind speed and for initializing the vector components when scatterometers are not available. Since both reanalyses assimilate scatterometers, their surface fields should be constrained by scatterometers to some degree. However, they differ from QuikSCAT. The near-surface convergence/divergence fields from the two reanalyses on 22 August 2009 are shown in Figures 9d and 9e, respectively. Similar filamentary structures are evidenced, but the magnitude is weaker and spatial details are not only smoother but also different. It can be noted that ERA-Interim is dictated mostly by convergence (positive) filaments, and the divergence (negative) filaments that are so ubiquitous in OAF flux (Figure 9a) and scatterometers (Figures 9c and 9d) are hardly seen. CFSR, though produced both convergence and divergence filaments, is contaminated by the spurious oscillations of small-scale convergence and divergence at low and midlatitudes. This appears to be the artifacts of the Gibbs ripples [Navarra *et al.*, 1994]. The differences in surface wind convergence/divergence daily fields between OAF flux and the reanalyses suggest that the methodology and approaches in use affect the fidelity of wind derivatives, even though the scatterometers were the input data sets in all three products. The OAF flux synthesis is statistically based, multisensor combination, and the resultant surface wind fields are subject to the satellite data coverage and also the number of available sensors. On the other hand, the reanalysis depends on the model physics to interpolate the observations assimilated into the model, and the resultant surface wind fields are subject, to a large degree, to the representation of the parameterization of the subgrid processes. Hence, spatial resolution becomes important for the reanalysis, as the smoother ERA-Interim field may be related to the coarser spatial resolution of 0.7° compared to 0.3° for CFSR and 0.25° for OAF flux.

The daily mean fields examined in Figures 9a–9d fall at a time when both QuikSCAT and ASCAT were available. For the years before September 1999, there was no influence of scatterometer on the OAF flux, albeit both ERA-Interim and CFSR assimilated ERS-1/2. It would thus be interesting to see whether the frontal-scale filaments still exist in the OAF flux. For this purpose, the daily mean field on 25 August 1998 was chosen, as on that day there was a category-3 storm, Hurricane Bonnie, heading toward north and northwest in the North Atlantic. The daily mean global convergence/divergence fields from the OAF flux and the two reanalyses are shown in Figures 10a–10c, respectively. Interestingly, the findings are similar to those shown in Figures 9a–9d. All the three products have captured the synoptic convergence/divergence filaments, but they differ in the spatial details. The OAF flux shows the filaments in the form of convergence-divergence couplets, which is different from ERA-Interim that is dominated mostly by the convergence (positive) filaments. CFSR has a stronger divergence component compared to ERA-Interim, but the Gibbs ripples in the

low and midlatitudes (Figure 9e) have a similar contamination effect on the global field. The differences between the satellite-based synthesis and atmospheric reanalyses indicate that much still needs to be learned about the structure and physics of the frontal-scale air-mass convergence in the midlatitudes.

Differences between the OAFflux and the reanalyses are substantial during severe storm events for the pre-QuikSCAT period. The surface convergence/divergence fields in the Northwest Atlantic area are enlarged to close-up the near-surface fields associated with Hurricane Bonnie (Figures 10d–10f). All three products are similar in depicting the northwestward orientation of the storm but vary considerably in constructing the structure of the storm center. While the two reanalyses produced a slanted blob of high surface convergence with slight variation in magnitude, the OAFflux constructed a field with much richer detail, featuring the storm's eye (i.e., the small area of divergence in the middle of convergence), the eyewall (i.e., the intense convergence surrounding the eye), and the disintegrated divergence clusters to the northeast of the storm. In summary, compared to ERA-Interim and CFSR, the spatial details of surface convergence/divergence associated with the synoptic storm systems and mesoscale fronts are depicted by the OAFflux for both the pre and post-QuikSCAT periods.

7. Summary

A high-resolution global analysis of daily ocean surface vector winds that covers the satellite wind observing period, from the first launch of SSM/I in July 1987 to the present, was developed by the Objectively Analyzed air-sea Heat Fluxes (OAFflux) project. The time series was merged from 12 satellite sensors, including two scatterometers (QuikSCAT and ASCAT) and 10 passive microwave radiometers (AMSRE, six SSM/I series, two SSMIS series, and the passive polarimetric microwave radiometer from WindSat (only wind speed retrievals were used)). This study addressed main issues related to merging scatterometers with radiometers to create a long-term time series for surface vector winds. These issues include the rationale that supports the synergy of scatterometers and radiometers, the methodology and strategy that were employed for the OAFflux objective synthesis, the challenges that were encountered during the synthesis, and the quality of the OAFflux synthesized daily mean fields with reference to scatterometers and atmospheric reanalyses.

The study investigated the practical bases for synergizing scatterometer and radiometers. Existing literature indicates that scattering and emission from the sea surface both describe the electromagnetic wave diffraction from surface short-scale waves that generate surface roughness. Our analysis showed that, on an annual basis, high winds account for a mere 2% over the global field, and low winds and moderate winds for about 20% and 78%, respectively. Our analysis also showed that scatterometer and radiometer products have high consistency in the low and moderate wind speed range, but bifurcate in the high wind speed range. That low and moderate winds constitute 98% of global daily wind fields and are the range of winds better retrieved by both scatterometers and radiometers establishes the base for integrating the two types of sensors to create a unified surface vector wind product.

The methodology of the OAFflux objective synthesis is based on the theory of the least-variance linear statistical estimation, which leads to the formulation of a least squares estimator (the so-called cost function) to include not only data from different sources but also a priori information to constrain the solution. The cost function of the OAFflux synthesis has two sets of constraints. One is that the analyzed zonal (u) and meridional (v) winds, and wind speed $w = \sqrt{u^2 + v^2}$ should be as close as possible to satellite retrievals and input background information in a least squares sense, and the other is that the solution of (u, v) should satisfy a set of kinematic constraints such as vorticity and divergence conservations. ERA-Interim and CFSR provided the background information that is needed for two occasions: (i) initialization of wind direction when there are no scatterometer measurements prior to 1999, and (ii) gap-filling of missing values in satellite observations. The minimization process seeks a best fit of daily wind field that satisfies the data constraints within the specified weight matrices.

The study showed that the most challenging issue for the OAFflux multisensor synthesis is the construction of the near-surface circulation associated with synoptic weather storms. Three factors contribute to the challenge. One is the lack of passive microwave radiometer wind speed retrievals in rain conditions, which reduces satellite data coverage for the synoptic weather systems. The second is that the removal of the rain-contaminated wind vector cells in QuikSCAT creates data voids that cannot be easily filled by the reanalysis winds due to their lack of spatial variability. The third factor is that the differences between KNMI

ASCAT and RSS QuikSCAT wind speeds at high-wind conditions are difficult to reconcile particularly when a fast-moving synoptic system is involved. The sensitivity experiments conducted by OAFlux showed that, while the synthesized daily mean wind fields are barely affected by the interscatterometer differences on the basin scales, the magnitude and structural details of the winds associated with synoptic weather systems are, however, scatterometer-dependent. This shows that the diverse microwave radiometer and scatterometer retrieval products can be combined in a complementary way to construct a daily mean wind vector, albeit high winds and heavy rain conditions are a challenge.

Wind derivatives amplify the errors in the wind products and compromise the signals. It is found that the structure of daily mean surface wind convergence/divergence field varies with product, owing perhaps to the different spectra possessed by different products [Vogelzang *et al.*, 2011]. Scatterometer daily surface convergence fields constructed on a 0.25° grid are too noisy to discern any meaningful spatial patterns; but after spatial filtering, mesoscale filaments of surface convergence/divergence and couplets are evidenced in regions associated with the ITCZ, SPCZ, and midlatitude surface fronts. The OAFlux daily mean fields show that the synthesis is capable of leaving out the grid size noises and the resultant convergence/divergence filaments and couplets have refined spatial details. On the other hand, the analysis of ERA-Interim shows that the frontal-scale details are not only smoother and weaker but also dominated primarily by the convergence filaments with limited divergence activities—with the cause yet to be understood. CFSR has a better depiction of the divergence filaments but the Gibbs ripples contaminate the global pattern. CFSR and ERA-Interim assimilated the scatterometers. The differences between the OAFlux synthesis and atmospheric reanalyses indicate that the satellite-derived (or assimilated) surface wind products are sensitive to the methodology and approach in use.

In summary, this part one study provided an insight on the practical use of the least-variance linear statistical estimation in producing a unified time series of ocean vector winds through merging scatterometers with passive microwave radiometers. We recognize that the daily resolution is a caveat for studies of the diurnal variability in surface winds. Nevertheless, as the global climate has been and continues to be changing, the scientific values of a continuous and consistent surface vector wind time series from 1987 onward can be significant in variety of ways, given that winds are involved in virtually every aspect of air-sea feedback and interaction. The confidence and sensitivity of the OAFlux time series to differences in satellite retrievals and to uncertainties caused by unresolved subdaily variability are to be addressed in an upcoming study.

Acknowledgments

The project is sponsored by the NASA Ocean Vector Wind Science Team (OVWST) activities under grant NNA10AO86G. The support and technical inputs from the international OVWST members during the 5 year development of the OAFlux wind synthesis products were acknowledged. The three anonymous reviewers were sincerely thanked for their thorough reviews and detailed and constructive comments that have helped greatly on the clarity and presentation of the manuscript. The OAFlux data sets are freely available from the project website at <http://oaflex.whoi.edu/>. The satellite wind products of SSM/I, SSMIS AMSR-E, and QuikSCAT were downloaded from the Remote Sensing Systems at <http://www.remss.com/>, and ASCAT data sets from NASA JPL PO.DAAC at <http://podaac.jpl.nasa.gov>. The original ASCAT data sets are hosted by KNMI at <http://www.knmi.nl/scatterometer>. ERA-Interim and CFSR reanalyses were downloaded from the NCAR Research Data Archive at <http://rda.ucar.edu>.

References

- ASCAT Wind Product User Manual (2013), Version 1.13, 23 pp., Ocean and Sea Ice SAF, The Royal Netherlands Meteorological Institute (KNMI), Utrecht, Netherlands. [Available at http://www.knmi.nl/scatterometer/publications/pdf/ASCAT_Product_Manual.pdf, last accessed May 2013]
- Atlas, R., R. N. Hoffman, S. C. Bloom, J. C. Jusem, and J. Ardizzone (1996), A multiyear global surface wind velocity dataset using SSM/I wind observations, *Bull. Am. Meteorol. Soc.*, *77*, 869–882.
- Atlas, R., R. N. Hoffman, J. Ardizzone, S. M. Leidner, J. C. Jusem, D. K. Smith, and D. Gombos (2011), A cross-calibrated, multiplatform ocean surface wind velocity product for meteorological and oceanographic applications, *Bull. Am. Meteorol. Soc.*, *92*, 157–174, doi:10.1175/2010BAMS2946.1.
- Attema, E. (1991), The active microwave instrument onboard the ERS-1 satellite, *Proc. IEEE*, *79*(6), 791–799.
- Bentamy, A., Y. Quilfen, and P. Flament (2002), Scatterometer wind fields: A new release over the decade 1991–2001, *Can. J. Remote Sens.*, *28*(3), 431–449.
- Bentamy, A., S. A. Grodsky, J. A. Carton, D. Croizé-Fillon, and B. Chapron (2012), Matching ASCAT and QuikSCAT winds, *J. Geophys. Res.*, *117*, C02011, doi:10.1029/2011JC007479.
- Bourassa, M. A., D. M. Legler, J. J. O'Brien, and S. R. Smith (2003), Seawinds validation with research vessels, *J. Geophys. Res.*, *108*(C2), 3019, doi:10.1029/2001JC001028.
- Brown, G. S. (1979), Estimation of surface wind speeds using satellite-borne measurements at normal incidence, *J. Geophys. Res.*, *84*(B8), 3974–3978.
- Brown, R. A. (2002), Scaling effects in remote sensing applications and the case of organized large eddies, *Can. J. Remote Sens.*, *28*, 340–345.
- Carswell, J. R., R. E. McIntosh, S. C. Carson, F. K. Li, G. Neumann, D. J. McLaughlin, J. C. Wilkerson, and P. G. Black (1994), Airborne scatterometers: Investigating ocean backscatter under low- and high-wind conditions, *Proc. IEEE*, *82*(12), 1835–1860.
- Cavaliere, D. J., C. L. Parkinson, P. Gloersen, J. C. Comiso, and H. J. Zwally (1999), Deriving long-term time series of sea ice cover from satellite passive-microwave multisensor data sets, *J. Geophys. Res.*, *104*(C7), 15,803–15,814.
- Chelton, D. B., and M. H. Freilich (2005), Scatterometer-based assessment of 10-m wind analyses from the operational ECMWF and NCEP numerical weather prediction models, *Mon. Weather Rev.*, *133*, 409–429, doi:10.1175/MWR-2861.1.
- Chin, T. M., R. F. Milliff, and W. G. Large (1998), Basin-scale, high wavenumber, sea surface wind fields from a multiresolution analysis of scatterometer data, *J. Atmos. Oceanic Technol.*, *15*, 741–763.
- Daley, R. (1991), *Atmospheric Data Analysis*, 457 pp., Cambridge Univ. Press, Cambridge, U. K.

- Dee, D. P., et al. (2011), The ERA-Interim reanalysis: Configuration and performance of the data assimilation system, *Q. J. R. Meteorol. Soc.*, *137*, 553–597, doi:10.1002/qj.828.
- DeMoss, J. D., and K. P. Bowman (2007), Changes in TRMM rainfall due to the orbit boost estimated from buoy rain gauge data, *J. Atmos. Oceanic Technol.*, *24*, 1598–1607, doi:10.1175/JTECH2082.1.
- Donelan, M. A., and W. J. Pierson (1987), Radar scattering and equilibrium ranges in wind-generated waves with application to scatterometry, *J. Geophys. Res.*, *92*(C5), 4971–5029.
- Draper, D. W., and D. G. Long (2004), Simultaneous wind and rain retrieval using Seawinds data, *IEEE Trans. Geosci. Remote Sens.*, *42*, 1411–1423.
- Ebuchi, N., H. C. Graber, and M. J. Caruso (2002), Evaluation of wind vectors observed by QuikSCAT/SeaWinds using ocean buoy data, *J. Atmos. Oceanic Technol.*, *19*, 2049–2069.
- Fangohr, S., and E. C. Kent (2012), An estimate of structural uncertainty in QuikSCAT wind vector retrievals, *J. Appl. Meteorol. Climatol.*, *51*, 954–961.
- Figa-Saldaña, J., J. J. W. Wilson, E. Attema, R. Gelsthorpe, M. R. Drinkwater, and A. Stoffelen (2002), The advanced scatterometer (ASCAT) on the meteorological operational (MetOp) platform: A follow on for European wind scatterometers, *Can. J. Remote Sens.*, *28*(3), 404–412.
- Freilich, M. H., and R. S. Dunbar (1999), The accuracy of the NSCAT-1 vector winds: Comparisons with NDBC buoys, *J. Geophys. Res.*, *104*(C5), 11,231–11,246.
- Freilich, M. H., and B. A. Vanhoff (2003), The relationship between winds, surface roughness, and radar backscatter at low incidence angles from TRMM precipitation radar measurements, *J. Atmos. Oceanic Technol.*, *20*, 549–562.
- Gaiser, P. W., et al. (2004), The WindSat spaceborne polarimetric microwave radiometer: Sensor description and early orbit performance, *IEEE Trans. Geosci. Remote Sens.*, *42*, 2347–2361.
- GCOS (2010), Implementation plan for the global observing system for climate in support of the UNFCCC, GCOS-138, 180 pp., Geneva, Switzerland. [Available at <https://www.wmo.int/pages/prog/gcos/Publications/gcos-138.pdf>]
- Hansen, J., M. Sato, and R. Ruedy (2012), Perception of climate change, *Proc. Natl. Acad. Sci. U. S. A.*, *109*(37), E2415–E2423.
- Hoffman, R. N. (1984), SASS wind ambiguity removal by direct minimization. Part II: Use of smoothness and dynamical constraints, *Mon. Weather Rev.*, *112*, 1829–1852.
- Hoffman, R. N., and S. M. Leidner (2005), An introduction to the near-real-time QuikSCAT data, *Weather Forecasting*, *20*, 476–493.
- Hoffman, R. N., S. M. Leidner, J. M. Henderson, R. Atlas, J. V. Ardizzone, and S. C. Bloom (2003), A two-dimensional variational analysis method for NSCAT ambiguity removal: Methodology, sensitivity, and tuning, *J. Atmos. Oceanic Technol.*, *20*, 585–605.
- Hollinger, J. P., J. L. Peirce, and G. A. Poe (1990), SSM/I instrument evaluation, *IEEE Trans. Geosci. Remote Sens.*, *28*(5), 781–790.
- Johnson, R. H., and P. E. Ciesielski (2013), Structure and properties of Madden-Julian oscillations deduced from DYNAMO sounding arrays, *J. Atmos. Sci.*, *70*, 3157–3179.
- Jones, W. L., L. C. Schroeder, D. H. Boggs, E. M. Bracalente, R. A. Brown, G. J. Dome, W. J. Pierson, and F. J. Wentz (1982), The SEASAT-A satellite scatterometer: The geophysical evaluation of remotely sensed wind vectors over the ocean, *J. Geophys. Res.*, *87*(C5), 3297–3317, doi:10.1029/JC087iC05p03297.
- Joyce, T. M., Y.-O. Kwon, and L. Yu (2009), On the relationship between synoptic wintertime atmospheric variability and path shifts in the Gulf Stream and Kuroshio Extension, *J. Clim.*, *22*(12), 3177–3192.
- Karagali, I., M. Badger, A. N. Hahmann, A. P. Diaz, C. B. Hasager, and A. M. Sempreviva (2013), Spatial and temporal variability of winds in the Northern European Seas, *Renewable Energy*, *57*, 200–210, doi:10.1016/j.renene.2013.01.017.
- Karagali, I., A. P. Diaz, M. Badger, and C. B. Hasager (2014), Wind characteristics in the North and Baltic Seas from the QuikSCAT satellite, *Wind Energy*, *17*(1), 123–140, doi:10.1002/we.1565.
- Katsura, S., E. Oka, B. Qiu, and N. Schneider (2013), Formation and subduction of North Pacific tropical water and their interannual variability, *J. Phys. Oceanogr.*, *43*, 2400–2415, doi:10.1175/JPO-D-13-031.1.
- Kelly, K. A., and S. Dong (2013), The contributions of atmosphere and ocean to North Atlantic subtropical mode water volume anomalies, *Deep Sea Res., Part II*, *91*, 111–127.
- Kelly, K. A., S. Dickinson, M. J. McPhaden, and G. C. Johnson (2001), Ocean currents evident in satellite wind data, *Geophys. Res. Lett.*, *28*(12), 2469–2472, doi:10.1029/2000GL012610.
- Konda, M., H. Ichikawa, and H. Tomita (2009), Wind speed and latent heat flux retrieved by simultaneous observation of multiple geophysical parameters by AMSR-E, *J. Remote Sens. Soc. Jpn.*, *29*, 191–198.
- Kunkee, D. B., G. A. Poe, D. J. Boucher, S. D. Swadley, Y. Hong, J. E. Wessel, and E. A. Uliana (2008), Design and evaluation of the first special sensor microwave imager/sounder, *IEEE Trans. Geosci. Remote Sens.*, *46*(4), 863–883.
- Laursen, B., and N. Skou (2001), Wind direction over the ocean determined by an airborne, imaging, polarimetric radiometer system, *IEEE Trans. Geosci. Remote Sens.*, *39*(7), 1547–1555.
- Legler, D. M., I. M. Navon, and J. J. O'Brien (1989), Objective analysis of pseudo-stress over the Indian Ocean using a direct minimization approach, *Mon. Weather Rev.*, *117*, 709–720.
- Lemaire, D., P. Sobieski, and A. Guissard (1999), Full-range sea surface spectrum in nonfully developed state for scattering calculations, *IEEE Trans. Geosci. Remote Sens.*, *37*, 1038–1051.
- Liu, W. T., and W. Tang (1996), Equivalent neutral wind, *Rep. 96-17*, 16 pp., Jet Propul. Lab. Publ., Pasadena, Calif.
- Mears, C. A., D. K. Smith, and F. J. Wentz (2001), Comparison of SSM/I and buoy-measured wind speeds from 1987–1997, *J. Geophys. Res.*, *106*(C6), 11,719–11,729.
- Meissner, T., and F. J. Wentz (2002), An updated analysis of the ocean surface wind direction signal in passive microwave brightness temperatures, *IEEE Trans. Geosci. Remote Sens.*, *40*(6), 1230–1240.
- Meissner, T., and F. J. Wentz (2012), The emissivity of the ocean surface between 6 and 90 GHz over a large range of wind speeds and Earth incidence angles, *IEEE Trans. Geosci. Remote Sens.*, *50*(8), 3004–3026.
- Milliff, R. F., J. Morzel, D. B. Chelton, and M. H. Freilich (2004), Wind stress curl and wind stress divergence biases from rain effects on QSCAT surface wind retrievals, *J. Atmos. Oceanic Technol.*, *21*, 1216–1231.
- Moller, D., P. D. Mourad, and S. J. Frasier (2000), Field observations of radar backscatter from the ocean surface under low wind speed conditions, *J. Geophys. Res.*, *105*(C10), 24,059–24,069, doi:10.1029/2000JC900103.
- Naderi, F., M. H. Freilich, and D. G. Long (1991), Spaceborne radar measurement of wind velocity over the ocean—An overview of the NSCAT system, *Proc. IEEE*, *79*(6), 850–866.
- Navarra, A., W. F. Stern, and K. Miyakoda (1994), Reduction of the Gibbs oscillation in spectral model simulations, *J. Clim.*, *8*, 1169–1183.

- Padia, K. (2010), *Oceansat-2 Scatterometer Algorithms for Sigma-0, Processing and Products Format*, Version 1.1, The Indian Space Research Organisation (ISRO), Bengaluru, India.
- Peterson, T. C., P. A. Stott, and S. Herring (2012), Explaining extreme events of 2011 from a climate perspective, *Bull. Am. Meteorol. Soc.*, *93*(7), 1041–1067.
- Phillips, O. M. (1957), On the generation of waves by turbulent wind, *J. Fluid Mech.*, *2*(5), 417–445.
- Plant, W. J. (1986), Two-scale model for short wind-generated waves and scatterometry, *J. Geophys. Res.*, *91*(C9), 10,735–10,749.
- Plant, W. J., D. E. Weissman, W. C. Keller, V. Hessany, K. Hayes, and K. W. Hoppel (1999), Air/sea momentum transfer and the microwave cross section of the sea, *J. Geophys. Res.*, *104*(C5), 11,173–11,191, doi:10.1029/1999JC00038.
- Poli, P., D. P. Dee, P. Berrisford, and J.-N. Thépaut (2010), Overview of satellite data assimilation in the ERA-Interim reanalysis, in *Proceedings of 2010 EUMETSAT Meteorological Satellite Conference*, 1–8 pp., EUMETSAT, Cordoba, Spain. [Available at http://eumeds.eumetsat.int/Home/Main/AboutEUMETSAT/Publications/ConferenceandWorkshopProceedings/2010/SP_2010129112551446?l=en.]
- Portabella, M., and A. Stoffelen (2001), Rain detection and quality control of seawinds, *J. Atmos. Oceanic Technol.*, *18*(7), 1171–1183.
- Portabella, M., and A. C. M. Stoffelen (2009), On scatterometer ocean stress, *J. Atmos. Oceanic Technol.*, *26*, 368–382, doi:10.1175/2008JTECH0578.1.
- Portabella, M., A. Stoffelen, W. Lin, A. Turiel, A. Verhoef, J. Verspeek, and J. Ballabrera-Poy (2012), Rain effects on ASCAT-retrieved winds: Toward an improved quality control, *IEEE Trans. Geosci. Remote Sens.*, *50*(7), 2495–2506.
- Quilfen, Y., B. Chapron, and D. Vandemark (2001), The ERS scatterometer wind measurement accuracy: Evidence of seasonal and regional biases, *J. Atmos. Oceanic Technol.*, *18*, 1684–1697.
- Quilfen, Y., C. Prigent, B. Chapron, A. A. Mouche, and N. Houti (2007), The potential of QuikSCAT and WindSat observations for the estimation of sea surface wind vector under severe weather conditions, *J. Geophys. Res.*, *112*, C09023, doi:10.1029/2007JC004163.
- Reynolds, R. W., T. M. Smith, C. Liu, D. B. Chelton, K. S. Casey, and M. G. Schlax (2007), Daily high-resolution blended analyses for sea surface temperature, *J. Clim.*, *20*, 5473–5496.
- Ricciardulli, L., and F. J. Wentz (2011), Reprocessed QuikSCAT (V04) wind vectors with Ku-2011 geophysical model function, *Rep. 043011*, 8 pp., Remote Sens. Syst., Santa Rosa, Calif.
- Romanou, A., et al. (2013), Natural air–sea flux of CO₂ in simulations of the NASA-GISS climate model: Sensitivity to the physical ocean model formulation, *Ocean Modell.*, *66*, 26–44.
- Saha, S., et al. (2010), The NCEP climate forecast system reanalysis, *Bull. Am. Meteorol. Soc.*, *91*, 1015–1057, doi:10.1175/2010BAMS3001.1.
- Schroeder, L. C., W. L. Jones, P. R. Schaffner, and J. L. Mitchell (1985), AAFE Radscat 13.9 GHz measurements and analysis: Wind speed signature of the ocean, *IEEE J. Oceanic Eng.*, *OE104*, 346–357.
- Skliris, N., R. Marsh, S. A. Josey, S. A. Good, C. Liu, and R. P. Allan (2014), Salinity changes in the World Ocean since 1950 in relation to changing surface freshwater fluxes, *Clim. Dyn.*, *42*, 709–736, doi:10.1007/s00382-014-213107.
- Sobieski, P. W., C. Craeye, and L. F. Bliven (1999), Scatterometric signatures of multivariate drop impacts on fresh and salt water surfaces, *Int. J. Remote Sens.*, *20*, 2149–2166.
- Spencer, M. W., C. Wu, and D. G. Long (2000), Improved resolution backscatter measurements with the SeaWinds pencil-beam scatterometer, *IEEE Trans. Geosci. Remote Sens.*, *38*(1), 89–104.
- Stiles, B., and S. Yueh (2002), Impact of rain on wind scatterometer data, *IEEE Trans. Geosci. Remote Sens.*, *40*, 1973–1983.
- Stoffelen, A., and D. Anderson (1997), Ambiguity removal and assimilation of scatterometer data, *Q. J. R. Meteorol. Soc.*, *123*, 491–518.
- Sun, N., and F. Weng (2008), Evaluation of special sensor microwave imager/sounder (SSMIS) environmental data records, *IEEE Trans. Geosci. Remote Sens.*, *46*(4), 1006–1016.
- Syed, T. H., J. S. Famiglietti, D. P. Chambers, J. K. Willis, and K. Hilburn (2010), Satellite-based global-ocean mass balance estimates of inter-annual variability and emerging trends in continental freshwater discharge, *Proc. Natl. Acad. Sci. U. S. A.*, *107*(42), 17,916–17,921.
- Talagrand, O. (1997), Assimilation of observations, an introduction, *J. Meteorol. Soc. Jpn.*, *75*, 191–209.
- Tournadre, J., and Y. Quilfen (2005), Impact of rain cell on scatterometer data: 2. Correction of seawinds measured backscatter and wind and rain flagging, *J. Geophys. Res.*, *110*, C07023, doi:10.1029/2004JC002766.
- Trenberth, K. E., and J. T. Fasullo (2012), Tracking Earth's energy: From El Niño to global warming, *Surv. Geophys.*, vol. 33, 3(4).
- Verhoef, A., and A. Stoffelen (2012), OSCAT winds validation report, Version 1.0, *Tech. Note SAF/OSI/CDOP2/KNMI/TEC/RP/196*, 14 pp., EUMETSAT, The Royal Netherlands Meteorological Institute (KNMI), Utrecht, Netherlands. [Available at http://www.knmi.nl/publications/fulltexts/oscat_validation_1.0.pdf.]
- Vogelzang, J., A. Stoffelen, A. Verhoef, J. de Vries, and H. Bonekamp (2009), Validation of two-dimensional variational ambiguity removal on SeaWinds scatterometer data, *J. Atmos. Oceanic Technol.*, *26*, 1229–1245, doi:10.1175/2008JTECH11232.1.
- Vogelzang, J., A. Stoffelen, A. Verhoef, and J. Figa-Saldaña (2011), On the quality of high-resolution scatterometer winds, *J. Geophys. Res.*, *116*, C10033, doi:10.1029/2010JC006640.
- Weissman, D. E., W. J. Plant, W. C. Keller, and V. G. Irisov (2002), Comparison of scatterometer and radiometer wind vector measurements, *J. Atmos. Oceanic Technol.*, *19*, 100–113.
- Weissman, D. E., B. W. Stiles, S. M. Hristova-Veleva, D. G. Long, D. K. Smith, K. A. Hilburn, and W. L. Jones (2012), Challenges to satellite sensors of ocean winds: Addressing precipitation effects, *J. Atmos. Oceanic Technol.*, *29*, 356–374, doi:10.1175/JTECH-D-11-00054.1.
- Wentz, F. J. (1975), A two-scale scattering model for foam-free sea microwave brightness temperatures, *J. Geophys. Res.*, *80*(24), 3441–3446.
- Wentz, F. J. (1997), A well-calibrated ocean algorithm for SSM/I, *J. Geophys. Res.*, *102*(C4), 8703–8718.
- Wentz, F. J. (2013), SSM/I Version-7 calibration report, *Rep. 011012*, 46 pp., Remote Sens. Syst., Santa Rosa, Calif.
- Wentz, F. J., P. D. Ashcroft, and C. L. Gentemann (2001), Post-launch calibration of the TRMM microwave imager, *IEEE Trans. Geosci. Remote Sens.*, *39*(2), 415–422.
- Yu, L. (2007), Global variations in oceanic evaporation (1958–2005): The role of the changing wind speed, *J. Clim.*, *20*, 5376–5390.
- Yu, L. (2011), A global relationship between the ocean water cycle and near-surface salinity, *J. Geophys. Res.*, *116*, C10025, doi:10.1029/2010JC006937.
- Yu, L., and X. Jin (2012), Buoy perspective of a high-resolution global ocean vector wind analysis constructed from passive radiometers and active scatterometers (1987–present), *J. Geophys. Res.*, *117*, C11013, doi:10.1029/2012JC008069.
- Yu, L., and R. A. Weller (2007), Objectively analyzed air–sea heat fluxes (OAFlux) for the global ocean, *Bull. Am. Meteorol. Soc.*, *88*(5), 527–539.
- Yu, L., X. Jin, and R. Weller (2008), Multidecade global flux datasets from the objectively analyzed air–sea fluxes (OAFlux) project: Latent and sensible heat fluxes, ocean evaporation, and related surface meteorological variables, *OAFlux Project Tech. Rep. OA-2008-01*, 64 pp.

- Yueh, S. H., and J. Chubell (2012), Sea surface salinity and wind retrieval using combined passive and active L-band microwave observations, *IEEE Trans. Geosci. Remote Sens.*, *50*(4), 1022–1032.
- Yueh, S. H., R. Kwok, and S. V. Nghiem (1994), Polarimetric scattering and emission properties of targets with reflection symmetry, *Radio Sci.*, *29*, 1409–1420.
- Yueh, S. H., W. J. Wilson, F. K. Li, S. Y. Nghiem, and W. B. Ricketts (1995), Polarimetric measurements of the sea surface brightness temperature using an aircraft K-band radiometer, *IEEE Trans. Geosci. Remote Sens.*, *33*(1), 85–92.
- Yueh, S. H., B. W. Stiles, W.-Y. Tsai, H. Hu, and W. T. Liu (2001), QuikSCAT geophysical model function for tropical cyclones and applications to Hurricane Floyd, *IEEE Trans. Geosci. Remote Sens.*, *39*, 2601–2612.